DOE/GO/10093--T3

# INCIDENCE ANGLE MODIFIERS IN CYLINDRICAL SOLAR COLLECTOR DESIGN

RECEIVED
APR 27 1998
OSTI

FINAL REPORT FOR THE PERIOD
June 1996 - May 1997

Joseph P. Ryan

Solar Energy Applications Laboratory
Colorado State University
Fort Collins, CO 80523

DISTRIBUTION OF THIS DOCUMENT IS UNLIMITED

MASTER

Date Published: May 1997

PREPARED FOR THE U.S. DEPARTMENT OF ENERGY
CONSERVATION AND RENEWABLE ENERGY

Under Grant DE-FG36-95GO10093

# DISCLAIMER

THESIS

# INCIDENCE ANGLE MODIFIERS IN CYLINDRICAL SOLAR COLLECTOR DESIGN

Submitted by

Joseph P. Ryan

Department of Mechanical Engineering

In partial fulfillment of the requirements

for the degree of Master of Science

Colorado State University

Fort Collins, Colorado

Spring 1997

## ABSTRACT OF THESIS

# INCIDENCE ANGLE MODIFIERS IN CYLINDRICAL SOLAR COLLECTOR DESIGN

This thesis presents an analysis of the thermal performance of cylindrical solar collectors. A major contributor to performance is optics, the principle focus of this work. A tool used to compute the incidence angle modifiers (IAM's) for cylindrical solar collectors is presented. The Monte Carlo Method is employed in a Fortran 90 computer code to compute the hemispheric IAM's of cylindrical solar collectors. Using concentric cylinders, the tubes are modeled with and without back plane reflectors of varying size. The computed IAM's are verified both analytically and experimentally. Outdoor experiments on an array of cylindrical tubes with various back planes and two different tube spacings are described. Agreement with TRNSYS runs in daily energy gain is excellent. Over the 38 data sets, taken on different days, a maximum error of 11.2% is observed, with an average error of 3%. Heat loss tests, used to calculate an overall heat loss coefficient for the collector, are also described.

A parametric variation study is used to illustrate the effect of varying many of the collector parameters. This study provides insight into the significant design parameters for cylindrical solar collectors. This insight is used to analyze the effect of these design parameters on the annual energy delivered by the collector. In addition, a simple cost analysis illustrates the benefits of varying the design parameters. The use of this new program and a detailed Life Cycle Cost analysis are the tools needed for optimizing the design of a cylindrical solar collector.

The IAM code, executables, sample input and output files and instruction manual can be found on the world wide web: http://www.ColoState.EDU/Orgs/SEAL/research/IAM/iam.html.

Joseph P. Ryan
Department of Mechanical Engineering
Colorado State University
Fort Collins, Colorado 80523
Spring 1997

# TABLE OF CONTENTS

CHAPTER 1 - INTRODUCTION

CHAPTER 2 - THEORETICAL FORMULATION

CHAPTER 3 - MONTE CARLO MODEL

CHAPTER 4 - EXPERIMENTAL APPROACH

CHAPTER 5 - RESULTS AND DISCUSSION

CHAPTER 6 - CONCLUSIONS AND RECOMMENDATIONS

# LIST OF FIGURES

# LIST OF TABLES

# NOMENCLATURE

| | |
|---|---|
| $A$ | area [$m^2$] |
| $b_o$ | incident angle modifier coefficient |
| $C$ | convergence factor |
| $C_p$ | specific heat [kJ/kg-K] |
| $C_{tol}$ | convergence tolerance |
| $d$ | diameter [m, cm] |
| $\Delta E$ | change in energy [kJ] |
| $\Delta T$ | temperature difference [C, K] |
| $\Delta t$ | length of time step [s] |
| $\mathcal{E}$ | error |
| $\dot{E}$ | rate of energy change [W] |
| $e_x$, $e_y$, $e_z$ | direction cosines of emission direction relative to the Cartesian triad |
| $h_{rad}$ | radiation heat loss coefficient [$W/m^2$-C |
| $I$ | incident solar radiative flux [$W/m^2$] |
| $k_g$ | extinction coefficient of glass [$m^{-1}$] |
| $L$ | length of tube [m] |
| $m$ | mass of the fluid in the collector, mass of fluid delivered [kg] |
| $\dot{m}$ | mass flow rate of fluid through the collector [kg/s] |
| $N$ | number of tubes |
| $n$ | number of photons absorbed |
| $N_j$ | number of tank nodes in ICS |
| $n_g$ | index of refraction of glass |
| $p$ | tube pitch (on-center spacing) [m] |
| $P_{ann}$ | pressure in the annulus [Pa] |
| $Q_{coll}$ | simulated collector energy absorbed [kJ] |
| $Q_{deliv}$ | simulated collector energy delivered during a draw [kJ, kWh] |
| $q$ | collector energy gain or loss [kJ] |
| $\dot{q}$ | rate of collector energy gain or loss [W] |
| $R$, $R_n$ | random numbers |
| $r$ | reflectance of glass' outer surface |
| $r_i$ | radius of collector tube [m] |
| $r_o$ | radius of glass tube [m] |
| $r_d$ | diffuse weighting exponent |
| $r_{ss}$ | semi-specular weighting exponent |
| $S_{bp}$ | distance from backplane to tube center [m] |
| $T$ | temperature [C, K] |
| $T_N$ | temperature of node N in ICS |
| $t_g$ | thickness of glass [m] |

| | |
|---|---|
| $UA$ | heat loss coefficient [W/°C] |
| $V_{wind}$ | wind velocity [m/s] |
| $W_{bp}$ | width of backplane [m] |
| $x, y, z$ | Cartesian coordinates [m] |
| $x_e, y_e, z_e$ | emission location [m] |
| $x_i, y_i, z_i$ | photon intersection location [m] |
| $x_0, y_0, z_0$ | cylinder origin [m] |
| $\mathcal{Z}$ | cumulative normal distribution function |

**Greek**

| | |
|---|---|
| $\alpha$ | absorptance, solar altitude |
| $\beta$ | azimuthal angle about the specular reflection vector |
| $\Delta\theta$ | cone angle between specular direction and semi-specular direction |
| $\varepsilon_g$ | emissivity of the glass |
| $\phi$ | solar azimuth |
| $\theta$ | incident angle, polar angle |
| $\theta_2$ | angle of refraction |
| $\theta_l$ | longitudinal incident angle |
| $\theta_t$ | transverse incident angle |
| $\rho$ | reflectance |
| $\tau$ | transmittance |
| $\tau_a$ | transmittance only due to absorptance |
| $(\tau\alpha)$ | transmittance absorptance product |
| $(\tau\alpha)_d$ | diffuse transmittance absorptance product |
| $(\tau\alpha)_n$ | transmittance absorptance product at normal incidence |
| $\psi$ | azimuthal angle |

**Subscripts**

| | |
|---|---|
| amb | ambient |
| ann | annulus |
| ap | aperture plane |
| avg | average |
| back | back side of collector |
| beam | beam radiation |
| bp | backplane |
| cold | cold |
| coll | collector module, collected |
| d | diffuse |
| deliv | delivered |
| fin | final |
| flow | flow through collector |
| g | glass |

| | |
|---|---|
| hot | hot |
| i | incident, inside, intersection |
| in | inlet to collector |
| ini | initial |
| j | node number |
| l | longitudinal |
| len | length |
| loss | loss from collector |
| man | manifold |
| max | maximum |
| min | minimum |
| n | normal incidence |
| o | outgoing |
| out | outlet from collector |
| r | reflected |
| s | specular |
| sun | solar radiation |
| ss | semi-specular |
| t | transverse |
| tol | tolerance |
| top | top side of collector |
| tube | collector tube |
| 1,2 | refers to different media |
| $\parallel$ | parallel |
| $\perp$ | perpendicular |

## Abbreviations

| | |
|---|---|
| IAM | incidence angle modifier |
| ICS | integral collector storage |

# CHAPTER 1 INTRODUCTION

## 1.1 Introduction

This thesis addresses the issues involved in predicting the performance of cylindrical solar collectors. Accurately predicting the performance of a solar collector is important for two reasons: (1) to aid in the design of the solar collector and (2) to determine the annual energy savings in different locales. The performance of solar collectors varies throughout the day due to the varying angle at which the solar radiation is incident upon the collector. As a result, accurately predicting the performance of a solar collector requires the knowledge of how the collector performs relative to the solar radiation's angle of incidence. Incidence Angle Modifiers (IAM's) are used to correct a solar collector's performance at normal incidence to off normal directions. The typical flat plate collector achieves its optimal performance at normal incidence. The reduction in performance of flat plate collectors at off-normal incidence is primarily due to the optical properties of the glazing and collector plate. IAM's are defined by:

$$\mathrm{IAM} = \frac{(\tau\alpha)}{(\tau\alpha)_n} \tag{1.1}$$

the ratio of the transmittance-absorptance product, $(\tau\alpha)$, at a given angle of incidence to that at normal incidence, $(\tau\alpha)_n$. The $(\tau\alpha)$ describes the portion of solar radiation absorbed by the solar collector, relative to that incident upon the collector's aperture plane. IAM's for flat-plate collectors can reliably be calculated using an analytical and experimental approach [Duffie and Beckman, 1991]. An equation of the form:

$$\mathrm{IAM} = 1 + b_0\left(\frac{1}{\cos\theta} - 1\right) \tag{1.2}$$

is used where $b_0$ is called the *incidence angle modifier coefficient* and is determined experimentally [Smith, 1997]. The angle of incidence, $\theta$, is the angle between the incident radiation and the collector's outward normal.

Cylindrical solar collectors pose a more daunting problem. The more complex geometry of these collectors requires three-dimensional consideration. A pair of incident angles, referred to as theta longitudinal ($\theta_l$) and theta transverse ($\theta_t$), shown in Fig. 1.1 are used to characterize the angle of incidence of the sun's rays relative to the collector,. In

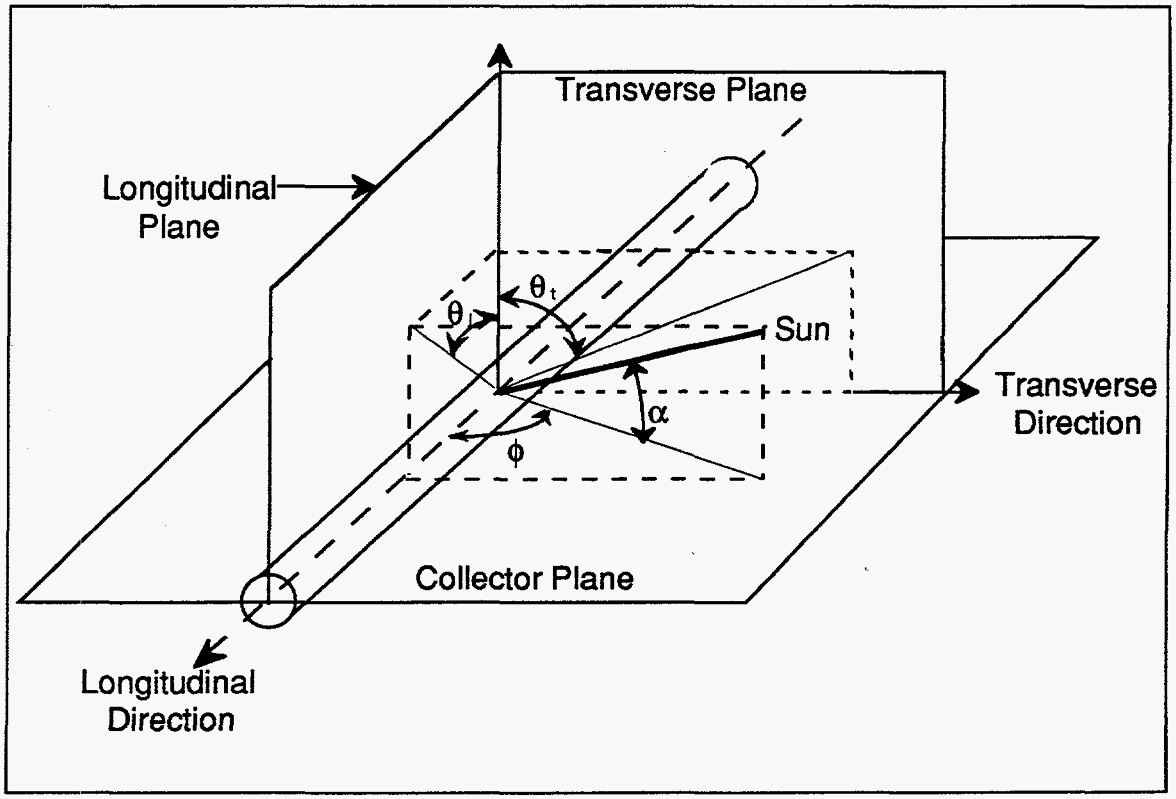

**Figure 1.1** Asymmetrical Incident Angles ($\theta_l$,$\theta_t$).

addition to material properties, the IAM's for cylindrical solar collectors must consider shading effects, inter-tube reflections and back plane reflectance. The $(\tau\alpha)$ is calculated for cylindrical solar collectors as

$$(\tau\alpha) = \frac{\sum n_{tubes}}{\sum n_{ap}} \tag{1.3}$$

the ratio of the number of photons absorbed by all collector tubes ($n_{tubes}$) to the number of photons directly incident upon the aperture plane ($n_{ap}$). Accurate prediction of the performance of cylindrical solar collectors provides the ability to calculate the performance of the system with respect to tube spacing and backplane reflectance.

## 1.2 Background

Several approaches have been used in the past to determine the optical performance of cylindrical solar collectors. Window and Zybert [1981] used a Monte Carlo program to compute the collection efficiency for concentrically arranged cylindrical solar collectors above diffuse reflectors of various shapes. The optical properties of the surfaces varied with incidence angle and second-chance processes (absorption of photons already reflected) were possible. The problem was simplified by neglecting end and edge effects (cylinders were infinite in length and number). Incident radiation was considered to be one of four types:

- normal incidence
- hemispherical incidence (diffuse)
- arc incidence across the tubes (transverse plane)

- arc incidence along the tubes (longitudinal plane)

This approach provided a general idea of collector performance, however it did not produce results at specific incidence angles, other than normal incidence. Collector geometries could be compared relative to one another but accurately predicting the performance of specific collectors was not possible.

Other early methods used biaxial IAM's to determine the optical efficiency. The biaxial incidence angles are contained in either the longitudinal plane $(\theta_l,0)$ or the transverse plane $(0,\theta_t)$ as shown in Fig. 1.1. McIntire [1982] approximated hemispherical IAM's for cylindrical collectors equipped with nonimaging, cusp concentrating reflectors. After calculating the biaxial IAM's, he used the multiplicative method to determine the hemispheric IAM's:

$$\mathrm{IAM}(\theta_l,\theta_t) = \mathrm{IAM}(\theta_l,0)\cdot \mathrm{IAM}(0,\theta_t) \tag{1.4}$$

Although this method produces an accurate approximation of hemispheric IAM's for concentrating cusp reflectors, Knapmiller [1991] and Menon [1994] have shown that it is inaccurate for low concentration (planar) backplane reflectors.

Theunissen and Beckman [1985] introduced a method for evaluating the optical performance of evacuated tube collectors. Their geometry consisted of an evacuated tube containing either a cylindrical absorber or a flat absorber. They used a mirrored wall approach, similar to Window and Zybert's, to simplify the problem. Again the collector module was infinite in both the longitudinal and transverse directions. The biaxial IAM's were computed and McIntire's multiplicative method was used to calculate the hemispherical IAM's. They use a ray-tracing procedure to determine the partition matrix between light sources (beam, sky diffuse, etc.) and light sinks (absorber, glass cover, etc.). Since the backplane was assumed to be a diffusely emitting, uniform light source, the tube pitch and backplane to tube spacing had to meet certain requirements. Also the absorber was assumed to be perfectly absorbing. Again, McIntire's multiplicative method was used to calculate the hemispherical IAM's.

A three-dimensional Monte Carlo program was developed by Knapmiller [1991] to compute IAM's for various geometries, including cylindrical collectors. Knapmiller used constructive solid geometry to represent the collector in three dimensions. Although the results are believed accurate, three inadequacies exist with this program: (1) the code is very slow, requiring several hours on a Sun SPARC 10 to obtain 1% convergence for 50 incidence angles, (2) it is difficult to construct and alter the geometry, and (3) using material models with more realistic directional distributions for reflections (i.e. Lambertian) produces inconsistent results.

Perez et al. [1995] introduced an analytical algorithm for calculating the amount of radiation received by cylindrical solar collectors. This approach differs from Theunissen and Beckman's in that the collector array is finite in both the transverse and longitudinal directions. This algorithm takes into account the design parameters of the collector array, inter-tube shading and diffuse radiation from the surroundings and the support structure (back plane). The algorithm does not account for specular reflections from the back plane, variation of tube pitch within the collector array or radiation reflected from other cylinders or surfaces in the collector array.

## 1.3 Research Objectives

Flat plate solar collectors have opaque insulation on their backside. Cylindrical solar collectors on the other hand, have the ability to collect radiative energy from all sides of the absorber tubes. Menon [1994] concluded that significant enhancement of collector performance can be achieved with the use of backplane reflectors. Although much work has been done on computing the optical efficiency of cylindrical solar collectors, a simple, accurate, efficient tool has yet to be provided for predicting the optical performance of these collectors.

The objective of this research is twofold: (1) to produce a tool with a simple interface, that will quickly and accurately compute the matrix of hemispheric IAM's of cylindrical solar collectors, and (2) to exercise this tool to determine the optimal geometric configuration for a cylindrical solar collector. The radiative performance is determined by the geometry and optical properties of the absorbers, covers and back planes. In addition to performance characteristics of the collector, decisions also need to encompass the cost of the various collector components.

## 1.4 Approach

The first objective is to produce a tool for computing the IAM's for cylindrical solar collectors. A Fortran 90 computer code is developed to accomplish this. Similar to Knapmiller's approach, the Monte Carlo method is employed. Three-dimensional modeling of the collector's geometry is used to include end and edge effects. A simple input deck is used to specify the material properties, collector geometry and control information (i.e. convergence tolerance, matrix of incident directions, etc.). Realistic material models are used to predict the optical performance. Calculation efficiency is stressed to keep the code fast and portable. To verify the validity of the IAM's computed by this new code, a combination of analytical and experimental tests are performed. The experimental tests consist of eight different geometric configurations including four different back planes and two different tube pitches.

Once sufficient verification of the validity of the computed IAM's is determined, the optimization of a cylindrical solar collector can begin. Parametric variation is used to optimize the geometric configuration of the collector. Given a specific configuration, the hemispherical IAM's are computed. A TRNSYS model of the collector uses these IAM's to conduct an annual simulation.

## 1.5 Organization of Thesis

The next chapter describes the theoretical approach. Specifics about the geometry and material models are defined and explained. An energy balance is then applied to a cylindrical solar collector module. The TRNSYS energy balance equations are then illustrated. Finally the problem is stated by identifying the significant parameters for predicting the performance of cylindrical solar collectors. Chapter 3 outlines the model used to calculate IAM's for cylindrical solar collectors. The Monte Carlo method is described. This includes the use of random numbers in modeling the behavior of the material properties. The ray tracing procedure and convergence of results are then described. Chapter 4 describes the experimental approach used to verify the validity of the computed IAM's. This includes a description of the system used in the experiments and the procedures used to help validate the computed IAM's. Chapter 5 provides results for the IAM program. First the results of the experimental study are given. Next the results of a parametric variation study of a cylindrical solar collector are outlined. An optimization procedure including annual TRNSYS simulations is discussed. Finally, Chapter 6 presents conclusions and recommendations for future research.

# CHAPTER 2 THEORETICAL FORMULATION

## 2.1 Introduction

This chapter provides a detailed analysis of the underlying theory for predicting the performance of cylindrical solar collectors. The equations governing the performance of cylindrical solar collectors are presented. First covered are descriptions of the collector's geometry and material properties. In addition an energy balance is applied to a cylindrical solar collector module. Finally, the significant parameters in the energy balance equation are identified.

## 2.2 Physical System

The geometry of the collector must be defined and represented in terms of the location, extent and orientation of each surface. Simple algebraic equations are used to define the collector's components. In order to facilitate portability and speed, the geometry of the collector is kept simple, with finite cylinders and planes as the only objects.

### 2.2.1 Geometry of Cylinders

Each collector tube is modeled as a pair of concentric cylinders, the outer of which is the glazing (Fig. 2.1). Any number of collector tubes can be modeled by the computer code. The tubes are aligned longitudinally along the x-axis as shown in Fig. 2.2. The

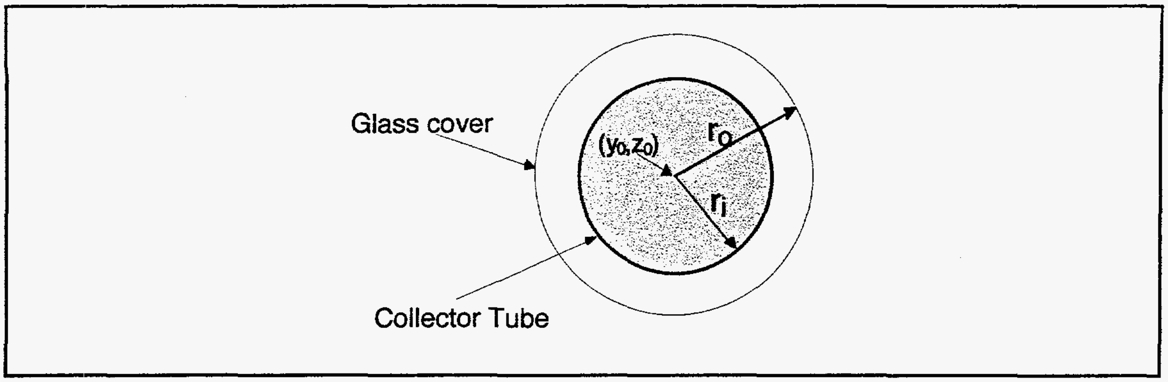

**Figure 2.1** Concentric Tube Geometry

orientation of the tubes is fixed, while the size and location are not. The size is given by three values: length (L), outside radius of the glazing ($r_o$), and outside radius of the collector tube ($r_i$), shown in Fig. 2.1. The location of each tube is determined by its origin ($x_0$, $y_0$, $z_0$), as shown in Fig. 2.2. For a typical array of collector tubes, $x_0$ and $z_0$ are constant for all cylinders and the displacement along the y-axis ($y_0$) varies.

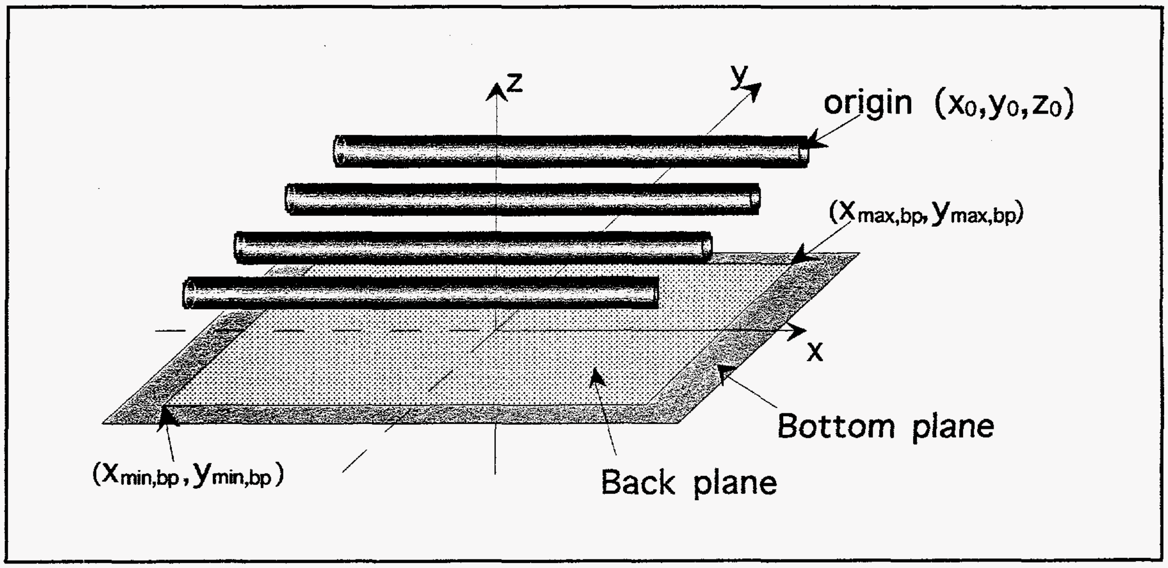

**Figure 2.2** Geometry of System.

### 2.2.2 Geometry of Planar Surfaces

In addition to the cylindrical surfaces, five planar surfaces are used in the emission and tracing of photons. These include the back plane, aperture plane, bottom plane, top plane, and emission plane.

A back plane is provided to model photon interaction behind the collector tubes. The back plane is rectangular and is situated in the x-y plane at z=0, with edges parallel to the x and y axes. The back plane is defined by the corner values, $(x_{min,bp}, y_{min,bp})$ and $(x_{max,bp}, y_{max,bp})$, to which its edges correspond (Fig. 2.2).

In addition to the back plane, an aperture plane must be specified. The aperture plane also lies in the x-y plane at z=0. Like the back plane, the size and location of the aperture plane are also defined by the corner values, $(x_{min,ap}, y_{min,ap})$ and $(x_{max,ap}, y_{max,ap})$. This virtual plane is used as a reference for determining the collector's performance. The $(\tau\alpha)$ is the ratio of energy absorbed by the collector tubes to the energy incident, in the absence of cylinders, upon the aperture plane, eqn. (1.3). The area of the aperture plane is often defined as:

$$A_{ap} = N \cdot L \cdot p \tag{2.1}$$

where N is the number of collector tubes, L is the length of the collector tubes and p is the average tube pitch (on-center spacing of the tubes). Since the aperture plane is simply a reference plane, keeping track of the specific area used for a particular set of IAM data is more important than adhering to a convention.

A bottom plane and top plane, both infinite in extent and parallel to the x-y plane, are used to absorb photons which have exited the volume of interest. The perfectly absorbing bottom plane is located at z=0, and absorbs photons reaching it and missing the backplane. The infinite, perfectly absorbing top plane is located at a z value just above the highest point on the collector and absorbs reflected photons traveling upwards which have missed the collector tubes.

Finally, an emission plane is used to emit the solar radiation incident upon the collector. This plane is rectangular with its upper and lower edges parallel to the bottom plane, shown in Fig. 2.3. It is oriented such that its surface normal strikes the bottom plane at the corresponding direction of incidence, shown in Fig. 2.3 as the solar azimuth ($\phi$) and solar altitude ($\alpha$), where these angles are relative to the Cartesian triad. It is just large enough to include all surfaces in its emissions. This is accomplished by first fitting a box around the collector tubes and projecting the three upper corners opposite the emission plane into the emission plane. The corners of the back plane are then projected into

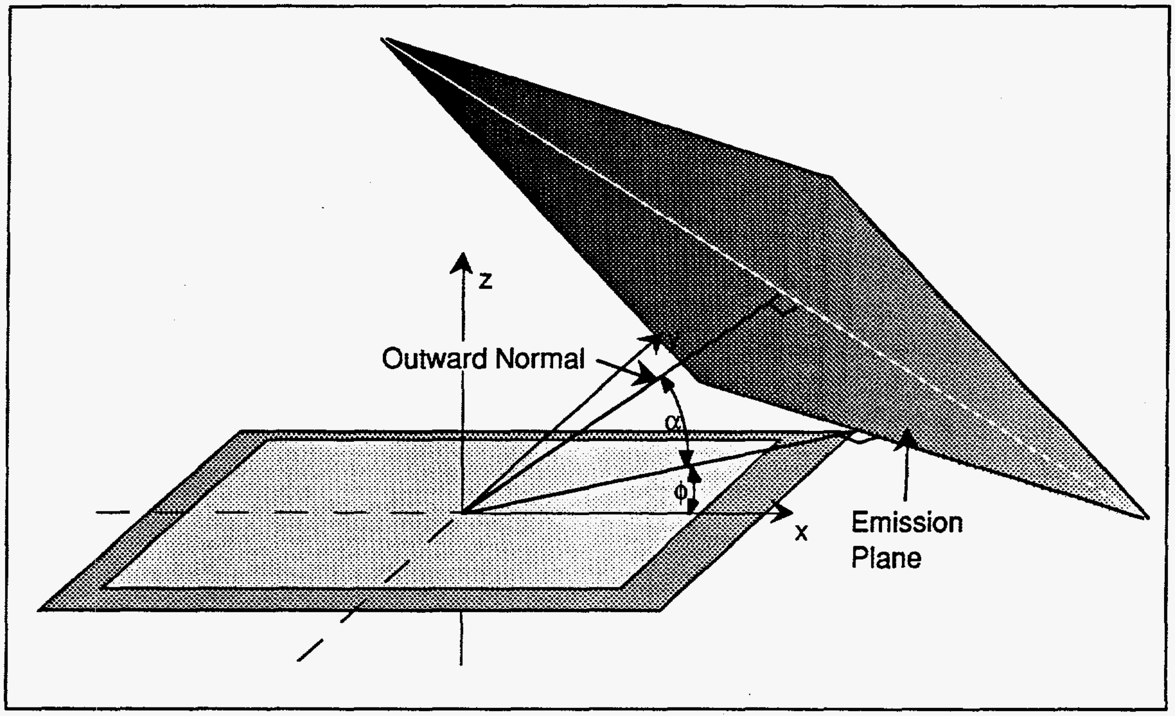

**Figure 2.3** Geometry of Emission Plane

the emission plane and the size of the emission plane is increased also to include these points. Finally the corner of the back plane nearest the emission plane is projected into the emission plane. The bottom edge of the emission plane then passes through this point. The plane pivots around either the corner of the back plane (as shown in Fig. 2.3) or the upper corner of the box nearest the emission plane, whichever puts it further from the origin. Photons are emitted at random locations across the emission plane and normal to its surface.

## 2.3 Material Properties

Each surface in the collector's geometry, excluding the emission, top, bottom and aperture planes, is assigned optical properties by virtue of its material type. Any number of material types can be defined and are divided into two categories: opaque surfaces and semi-transparent surfaces. Each collector tube is assigned a glass material and an absorber surface material. Sophisticated material properties are an unique feature of Monte Carlo photon tracing algorithms. Accurate modeling of the materials will produce more accurate results and material properties of arbitrarily high complexity can be defined. However, if material properties are too complex, run time increases and input becomes tedious. Thus, a compromise between these two factors is appropriate.

Here the primary simplification made is for all the material properties to be independent of the wavelength of the incident radiation. Since it is the sun's radiation which is being emitted, the radiative properties of the materials are assumed constant over the solar spectrum. As a result, average solar properties should be used for the surface materials.

### 2.3.1 Radiative Properties for Opaque Surfaces

Mixed material models, consisting of specular and diffuse components of reflectance, are typically used in Monte Carlo algorithms. This program extends the traditional mixed material model to be more representative of real materials. Specifically, two enhancements are proposed. First, a more sophisticated model for the outgoing directional distribution of "diffuse" reflections is proposed. Secondly, a semi-specular component, which "spreads" the specular reflection in space (motivated by Modest [1993]) is also proposed.

This particular implementation considers the radiative properties for opaque surfaces to be independent of incident angle. That is, the fraction of photons reflected diffusely and that reflected specularly remain constant, independent of incident angle of the incoming photon. Although this may lead to error in some cases, it was judged that insufficient material property data exist to warrant more than this level of modeling. If, after initial testing of this model, it is determined that more sophisticated models are required, it is a simple matter to implement them.

Figure 2.4 shows the three outgoing directional distributions for photons. Three components of reflectance are proposed. The first is a weighted diffuse component (Fig. 2.4a) with the outgoing reflectance flux described as:

$$\rho_d(\theta_0) = \rho_{d,n} \cos^{r_d - 1}(\theta_0) \tag{2.2}$$

An isotropic outgoing flux is obtained for $r_d = 0$. This is not a good model to use for most diffusely reflecting surfaces, since electromagnetic wave theory predicts zero emissivity at grazing angles for all surfaces [Modest, 1993]. The traditional Lambertian distribution

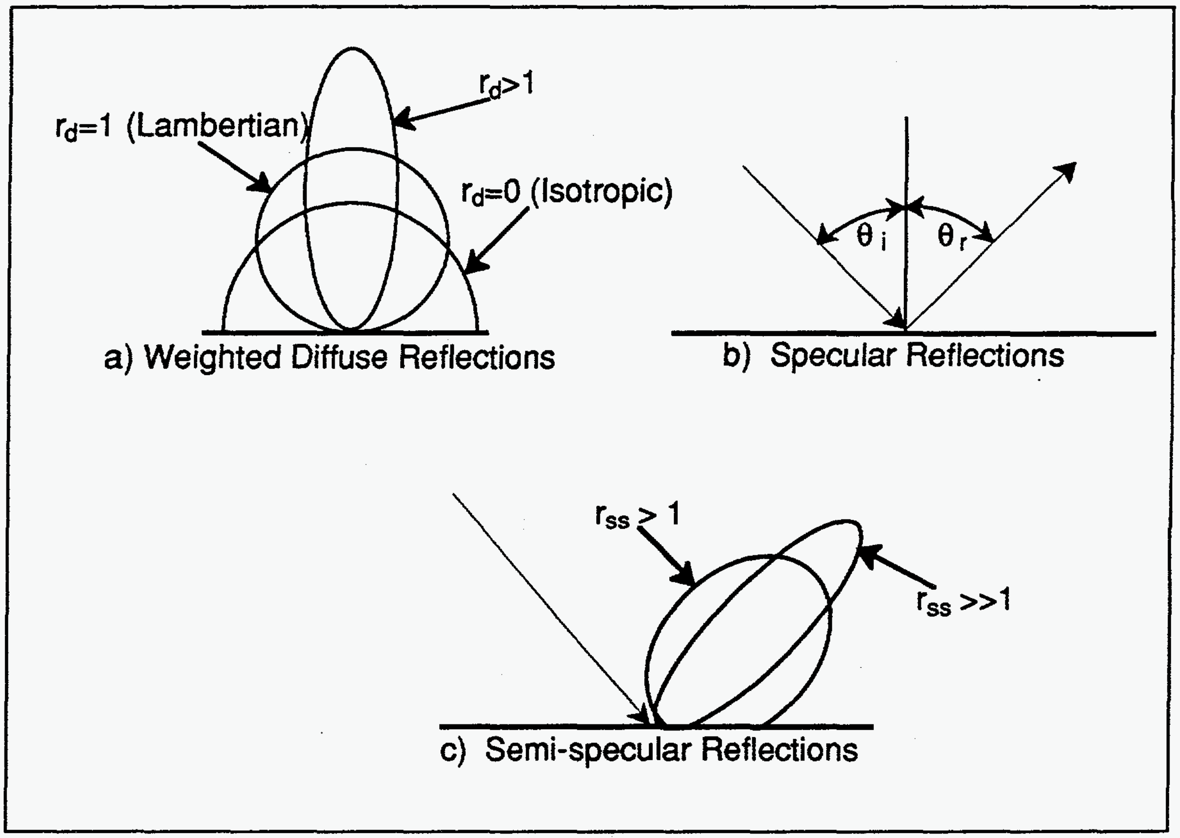

**Figure 2.4** Directional Distribution Components of Outgoing Reflectance

more closely follows electromagnetic wave theory and is obtained for $r_d = 1$. Powers of $r_d$ greater than 1 skew the distribution toward the normal, while powers of $r_d$ less than 1 skew the distribution toward the grazing angle.

The second outgoing directional distribution model is the traditional specular component (Fig. 2.4b). Specular reflections occur from optically smooth surfaces (e.g. polished metals, mirrors, glass, etc.). The reflected path, $(\theta_o,\phi_o)$, is related to the incident path, $(\theta_i,\phi_i)$, by:

$$\{\theta_o,\phi_o\} = \{\theta_i,\phi_i + \pi\} \tag{2.3}$$

The third and final outgoing directional distribution model is the semi-specular component. This represents the bidirectional reflection function described by Modest

[1993]. This component of reflectance exhibits a maximum at the specular direction, $\{\theta_0,\phi_0\}$ in eqn. (2.3), and the reflectance gradually diminishes away from the specular direction. In other words, semi-specular reflections are spread in space about the specular direction. Unpolished, yet relatively smooth metals produce reflections such as this. Similar to the weighted diffuse distribution, the semi-specular distribution is weighted with a value of $r_{SS}$. This exponent is used to control the spread of the semi-specular distribution. This is first accomplished by describing the reflection distribution about the surface normal, similar to eqn. (2.2):

$$\rho_{ss}(\theta_\perp) = \rho_{ss}\cos^{r_{ss}-1}(\theta_\perp) \tag{2.4}$$

This distribution is then rotated to the specular direction, scaled to go to zero at the grazing angle and eqn. (2.5) determines the cone angle between the specular direction and the actual reflection vector ($\Delta\theta$):

$$\Delta\theta = \left(\frac{\pi}{2} - \theta_i\right)\cdot\left|\theta_\perp - \frac{\pi}{4}\right|\cdot\frac{4}{\pi} \tag{2.5}$$

This distribution is then revolved about the specular direction using the random angle of revolution, $\beta$:

$$\theta_o = \theta_i + \Delta\theta\cdot\cos(\beta) \tag{2.6}$$

$$\phi_o = \phi_i + \pi + \Delta\theta\cdot\sin(\beta) \tag{2.7}$$

The effect of varying $r_{SS}$ is shown in Fig. 2.4c. As the value of $r_{SS}$ grows, the surface reflections become more specular in nature.

The overall reflectance (ρ) of a surface being modeled as a mixed material surface is the sum of the three components of reflectance:

$$\rho = \rho_s + \rho_d + \rho_{ss} \tag{2.8}$$

and the absorptance of the opaque material is the complement of the reflectance:

$$\alpha = 1 - \rho \tag{2.9}$$

These three components of reflectance provide the flexibility to simulate accurately many types of real surfaces.

### 2.3.2 Radiative Properties for Semi-transparent Surfaces

Before a photon can come into contact with an absorber tube, it must first penetrate the glass cover surrounding the tube. An approximate material model for glass is implemented in the Monte Carlo code for the sake of simplicity and performance. The approximation made is that the semi-transparent layer can be modeled locally as a flat plate, with no deviation from flight path due to refraction. This displacement due to refraction is illustrated in Fig. 2.5. This approximation becomes more accurate the thinner the layer of glass and the greater the tube diameter. In addition, over the hemisphere, the errors due to refraction will tend to cancel.

The radiative properties of glass vary significantly with the angle of incidence and are therefore calculated every 1° in incident angle. To aid in calculation efficiency, these values are stored in arrays and are linearly interpolated at incident angles in between these points. This precision was proven adequate by Burns and Pryor [1989]. At an incident

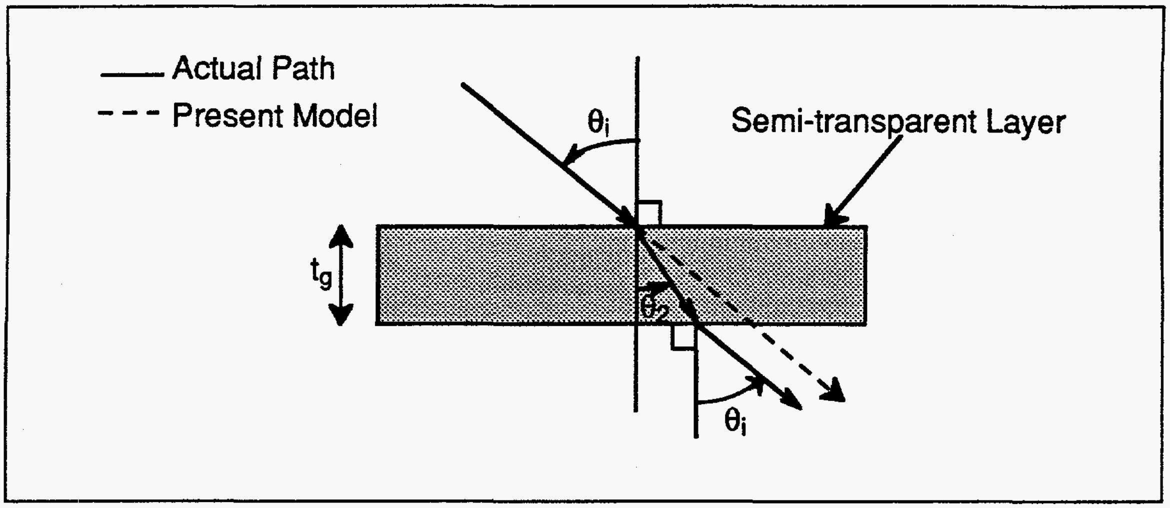

**Figure 2.5** Angle of Refraction ($\theta_2$) in a Semi-transparent Layer

angle of 90°, the reflectance of the glass is 1.0. With glass being a semi-transparent material, three radiative properties must be determined: transmittance ($\tau_g$), reflectance ($\rho_g$) and absorptance ($\alpha_g$). The user supplies the program with three glass properties which are used to calculate these three radiative properties. These are the index of refraction ($n_g$), the extinction coefficient ($k_g$) and the thickness of the glass ($t_g$).

The angle of refraction in the glass ($\theta_2$) is related to the angle of incidence ($\theta_i$) by Snell's law with an index of refraction for air of 1.0:

$$\theta_2 = \sin^{-1}\left(\frac{\sin\theta_i}{n_g}\right) \tag{2.10}$$

The reflectance of the glass' outer surface is then determined from Fresnel's equations for the reflection of unpolarized radiation from smooth surfaces:

$$r_\perp = \frac{\sin^2(\theta_2 - \theta_i)}{\sin^2(\theta_2 + \theta_i)} \tag{2.11}$$

$$r_{\parallel} = \frac{\tan^2(\theta_2 - \theta_i)}{\tan^2(\theta_2 + \theta_i)} \tag{2.12}$$

Of the radiation that is not reflected from the glass' outer surface, the portion transmitted (that which is not absorbed by the glass) is calculated from the extinction coefficient:

$$\tau_a = e^{\frac{-k_g t_g}{\cos\theta_2}} \tag{2.13}$$

The overall transmittance ($\tau_g$), including reflectance and absorptance, is found from ray-traces, as described in Duffie and Beckman [1991]:

$$\tau_{\perp} = \frac{(1 - r_{\perp})^2 \tau_a}{1 - r_{\perp}^2 \tau_a} \tag{2.14}$$

$$\tau_{\parallel} = \frac{(1 - r_{\parallel})^2 \tau_a}{1 - r_{\parallel}^2 \tau_a} \tag{2.15}$$

$$\tau_g = \frac{1}{2}\left(\tau_{\perp} + \tau_{\parallel}\right) \tag{2.16}$$

Similarly, the overall reflectance ($\rho_g$) of the glass cover is also found from ray-traces:

$$\rho_{\perp} = r_{\perp}\left[1 + \frac{(1 - r_{\perp})^2 \tau_a^{\ 2}}{1 - r_{\perp}^{\ 2} \tau_a^{\ 2}}\right] \tag{2.17}$$

$$\rho_{\parallel} = r_{\parallel}\left[1 + \frac{(1 - r_{\parallel})^2 \tau_a^{\ 2}}{1 - r_{\parallel}^{\ 2} \tau_a^{\ 2}}\right] \tag{2.18}$$

Assuming equal components of polarization:

$$\rho_g = \frac{1}{2}\left(\rho_{\perp} + \rho_{\parallel}\right) \tag{2.19}$$

The absorptance of the glass can be found using a similar approach, or it can simply be calculated from the relationship:

$$\tau_g + \rho_g + \alpha_g = 1 \tag{2.20}$$

The results of these equations are illustrated in Fig. 2.6. Thus, the glass properties account for the glass' being of finite thickness. Consequently, the approximations only involve the path, which is postulated to have a minimal effect.

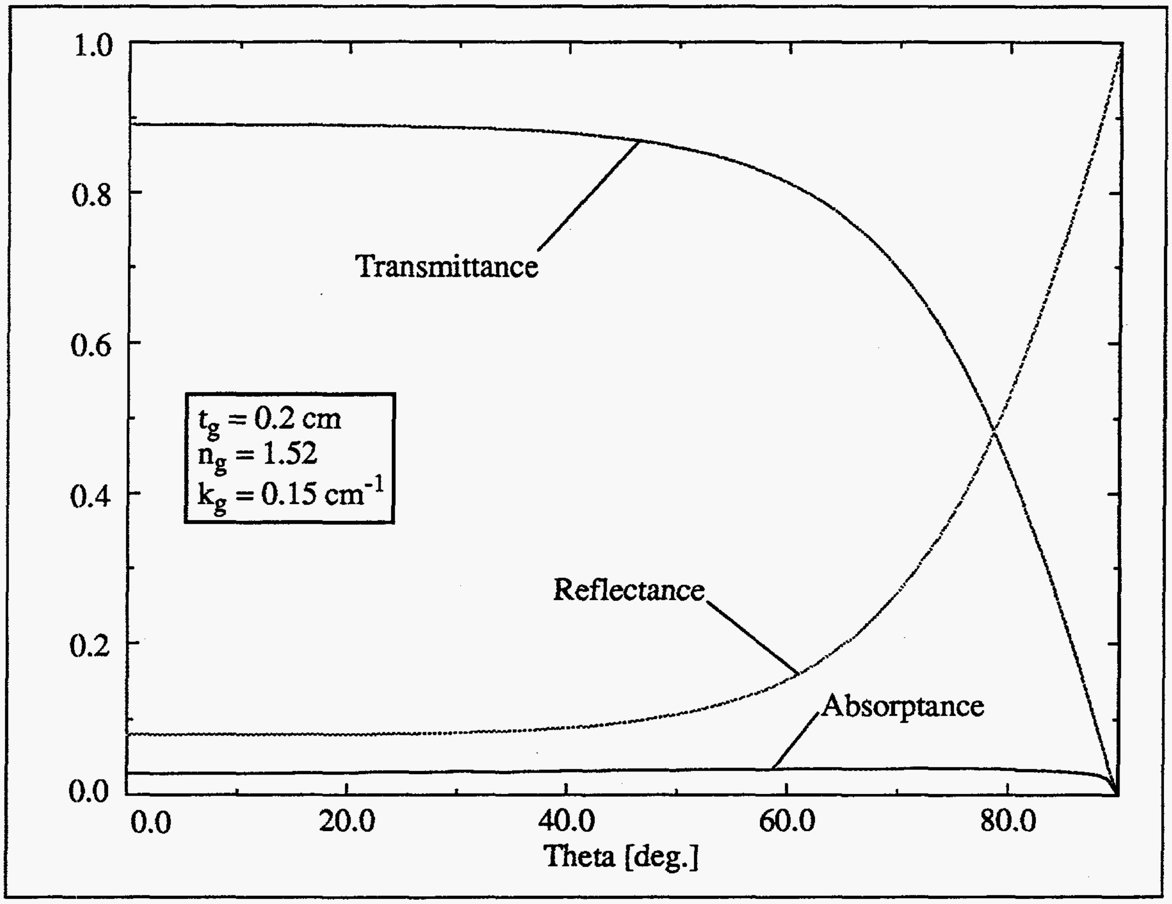

**Figure 2.6** Radiative Properties of Glass Relative to Incident Angle

As glass is an optically smooth surface, all reflections from the glass will follow the specular reflection path, eqn. (2.3).

## 2.4 Energy Balance Model

Applying an energy balance to a solar collector is a useful way of determining the significant performance parameters. Indeed, the thermal state of the solar collector is determined from an energy balance, permitting a simulation to be performed.

### 2.4.1 General Thermal Model

Consider a typical solar collector. The generic energy balance equation takes the form:

$$\dot{q}_{sun} = \dot{q}_{flow} + \dot{q}_{loss} + mC_p \frac{d\overline{T}}{dt} \tag{2.21}$$

the rate of energy gain from the sun ( $\dot{q}_{sun}$ ) is equal to the sum of the rate of energy gain by flow through the collector ( $\dot{q}_{flow}$ ), the rate of energy loss from the collector ( $\dot{q}_{loss}$ ) and the rate of change of energy of the collector ( $mC_p \frac{d\overline{T}}{dt}$ ), where $\overline{T}$ is the average collector temperature. This generic equation will be applied to a cylindrical solar collector. Most cylindrical solar collectors (with cylindrical absorbers) are Integral Collector Storage (ICS) units. The term ( $\dot{q}_{flow}$ ) is calculated as:

$$\dot{q}_{flow} = \dot{m}C_p(T_{out} - T_{in}) \tag{2.22}$$

When flow through the collector exists, it is usually important to account for temperature variation through the collector. However, this energy balance will be simplified by considering the collector module without flow ( $\dot{m} = 0$ ). Thus the rate of change of energy in the collector then reduces to:

$$\dot{E}_{coll} = mC_p \frac{dT}{dt} = \dot{q}_{sun} - \dot{q}_{loss} \tag{2.23}$$

The solar gains ( $\dot{q}_{sun}$ ) for a cylindrical solar collector are defined by:

$$\dot{q}_{sun} = (\tau\alpha) \cdot I_{beam} \cdot A_{ap} + \int_{\psi=0}^{2\pi} \int_{\theta=0}^{\frac{\pi}{2}} (\tau\alpha) I_d A_{ap} \sin\theta \cos\theta d\theta d\psi \tag{2.24}$$

where the $(\tau\alpha)$ is a function of incident angle, $(\theta_l, \theta_t)$, $I_{beam}$ is the incident beam radiation flux, $I_d$ is the incident isotropic diffuse radiation flux, and $A_{ap}$ is the aperture area. Equation (2.24) can be rewritten with the use of IAM's as:

$$\dot{q}_{sun} = IAM \cdot (\tau\alpha)_n \cdot I_{beam} \cdot A_{ap} + IAM_d \cdot (\tau\alpha)_n \cdot I_d \cdot A_{ap} \tag{2.25}$$

where $IAM_d$ is the diffuse IAM integrated over the hemisphere:

$$IAM_d = \int_{\psi=0}^{2\pi} \int_{\theta=0}^{\frac{\pi}{2}} IAM(\theta, \psi) \sin\theta \cos\theta d\theta d\psi \tag{2.26}$$

The losses for a cylindrical solar collector are very similar to the losses from a storage tank and are defined by:

$$\dot{q}_{loss} = UA_{coll}\left(\overline{T} - T_{amb}\right) \tag{2.27}$$

where $UA_{coll}$ is the overall heat loss coefficient for the collector, $\overline{T}$ is the average temperature of the fluid in the collector and $T_{amb}$ is the ambient temperature. The $UA_{coll}$ is a function of the UA of each collector tube ($UA_{tube}$) and the UA of the manifold ($UA_{man}$) which connects the tubes:

$$UA_{coll} = N \cdot UA_{tube} + UA_{man} \tag{2.28}$$

recalling that N is the number of tubes in the collector. The UA of the collector tubes is a function of the material properties of the tubes (glass and absorber), the properties of the annulus (gas or vacuum), and ambient conditions. The UA of the manifold is a function of the number of tubes, the tube pitch, the insulation used and ambient conditions.

### 2.4.2 TRNSYS Thermal Model

The TRNSYS Type 46 subroutine is used to simulate ICS modules. The energy balance equations used in this subroutine are similar to those described above. Similar to the TRNSYS tank model, the user specifies a number of nodes ($N_j$) into which the ICS is divided. TRNSYS performs an energy balance on each of these nodes at each time step. The following differential equation is used to describe the energy balance for node j at time t:

$$\frac{dT_j}{dt} = \frac{\dot{m}C_p\left(T_j - T_{j-1}\right) - q_{loss,j} + q_{sun,j}}{mC_p / N_j} \tag{2.29}$$

where $q_{loss,j}$ is the energy lost from node j and $q_{sun,j}$ is the solar gain for node j. The loss term is

$$q_{loss,j} = \frac{\left(UA_{top} + UA_{back}\right)\left(T_j - T_{amb}\right) + h_{rad}A_j\left(T_{g,j} - T_{sky}\right)}{N_j} \tag{2.30}$$

where $UA_{top}$ and $UA_{back}$ are the top and back components of the heat loss coefficient, $T_{sky}$ is the effective black-body sky temperature and $T_{g,j}$ is the glass temperature for node j. The radiation coefficient, $h_{rad}$, is determined by performing an energy balance on the glass cover and determining the temperature of the cover at each node ($T_{g,j}$). $T_{g,j}$ is parameterized as:

$$T_{g,j} = T_{g,j}\left(T_{sky}, T_{amb}, T_j, V_{wind}, \varepsilon_g, UA_{top}\right) \tag{2.31}$$

where $V_{wind}$ is the wind velocity and $\varepsilon_g$ is the emissivity of the glass cover. Smith [1997] shows that wind velocity is not a significant parameter in predicting the performance of solar collectors. Without knowing $T_{sky}$ and the ambiguity of the top and back components of the convection heat loss coefficient, the current model forces eqn. (2.30) to resemble eqn. (2.27) by setting $h_{rad} = 0$:

$$q_{loss,j} = UA_{coll}\left(T_j - T_{amb}\right) \tag{2.32}$$

Also, the tests are performed during the day, when the solar irradiation overwhelms the long-wave radiative losses. Then the TRNSYS energy model for each node is identical to the general model described in the previous sub-section, and the energy change equation for node j takes the form:

$$\dot{E}_j = A_{ap} \cdot (\tau\alpha)_n \cdot \left(IAM \cdot I_{beam,j} + IAM_d \cdot I_{d,j}\right) \tag{2.33}$$

where

$$I_{beam,j} = \frac{I_{beam} \cdot A_{ap}}{N_j} \tag{2.34}$$

$$I_{d,j} = \frac{I_d \cdot A_{ap}}{N_j} \tag{2.35}$$

Optical mode 4 is used in the TRNSYS Type-46 subroutine. This mode reads a matrix of longitudinal and transverse incidence angles and their corresponding IAM's. In

TRNSYS the solar radiation incidence angles are determined for the current time step, and bilinear interpolation is used to calculate the IAM at the current angle of incidence. In addition, eqn. (2.26) is used in TRNSYS to calculate $\mathrm{IAM_d}$.

## 2.5 Problem Parameterization

The purpose of this section is to identify the significant parameters for predicting the performance of cylindrical solar collectors. As stated in the previous section, the performance of ICS collectors is described by the change in internal energy of the collector itself. Therefore eqn. (2.23) is the equation of interest. Parameterizing this equation produces:

$$\dot{E}_{coll} = \dot{E}_{coll}\left(\dot{q}_{sun}, UA_{coll}\right) \tag{2.36}$$

Parameterizing eqn. (2.25) gives:

$$\dot{q}_{sun} = \dot{q}_{sun}\left(IAM, IAM_d, (\tau\alpha)_n, I_{beam}, I_d, A_{ap}\right) \tag{2.37}$$

Now, substituting eqn. (2.37) into eqn. (2.36) provides:

$$\dot{E}_{coll} = \dot{E}_{coll}\left(IAM, IAM_d, (\tau\alpha)_n, I_{beam}, I_d, A_{ap}, UA_{coll}\right) \tag{2.38}$$

All four design parameters (IAM, $(\tau\alpha)_n$, $A_{ap}$, $UA_{coll}$) are strongly dependent on the geometry and material properties of the collector, the focus of this paper. Using eqn. (1.1) as the definition of IAM's:

$$IAM = IAM\left\{(\tau\alpha), (\tau\alpha)_n\right\} \tag{2.39}$$

The $(\tau\alpha)$ can be parameterized as:

$$(\tau\alpha) = (\tau\alpha)\left\{\theta_l, \theta_t, p, n, L, \rho_{bp}, S_{bp}, W_{bp}, k_g t_g, n_g, d_g, \alpha_{tube}, d_{tube}\right\} \tag{2.40}$$

Finally, substituting eqn. (2.40) into eqn. (2.39) provides the following parameterization of IAM's:

$$IAM = IAM\left(\theta_l, \theta_t, p, N, L, \rho_{bp}, S_{bp}, W_{bp}, k_g t_g, n_g, r_o, r_i, \alpha_{tube}, d_{tube}\right) \tag{2.41}$$

The effect of varying many of these parameters will be illustrated in Chapter 5, Results and Discussion.

## 2.6 Summary

At this point the problem is clearly defined and formulated. Predicting the performance of cylindrical solar collectors reduces to predicting the change in energy of the collector. The previous section identified the significant parameters for predicting $\dot{E}_{coll}$. Of those parameters, the IAM's play a key role and are an area where significant improvements can be made. The next chapter describes the procedure used to calculate IAM's for cylindrical solar collectors.

# CHAPTER 3 MONTE CARLO MODEL

## 3.1 Introduction

This chapter describes the Fortran 90 computer code used to compute IAM's for cylindrical solar collectors. The primary objective of this computer code is to determine the absorbed fraction of photons, $(\tau\alpha)$, at any angle of incidence. Thermal radiation problems rarely have exact, closed form solutions. This can be seen for the problem at hand by examining the parameters involved in calculating IAM's for cylindrical solar collectors, eqn. (2.41). As a result, numerical methods are often used to obtain the solutions to these problems.

Generally, the more sophisticated a problem becomes, the more worthwhile the development of a Monte Carlo solution becomes [Modest, 1993]. Obviously for a simple problem with an analytical solution, the time required for development of the code would far exceed that required to solve the problem analytically. On the other hand, trying to find an analytical solution to a complicated set of integral equations, often requiring many assumptions, can be significantly more time consuming than developing a Monte Carlo code to solve the problem.

A computer code employing the Monte Carlo method is used to trace photon interactions in an enclosure. Here, the enclosure is formed by the infinite top and bottom planes. In particle Monte Carlo algorithms, particles are traced from "birth," or emission, to "death," or absorption, through possibly many intermediate reflections. Each particle represents a bundle of radiant energy, or photon bundle, hereinafter termed simply a photon. Each time the photon comes into contact with, or "hits," a surface, random numbers are used to determine the outcome (reflected, transmitted or absorbed) of the interaction. Once a photon has been absorbed, a new one is emitted. A sufficient number of photons must be emitted to render the answers stationary, or independent to some small statistical tolerance, of additional emissions.

Statistical methods can be used to solve many types of mathematical problems and require the use of random numbers. A roulette wheel is the classic provider of random numbers, hence the name Monte Carlo, the popular gambling city on the French Riviera. On the order of $10^5$ random numbers are needed to compute the $(\tau\alpha)$ at a single angle of incidence. The most efficient method of obtaining this many random numbers is to use the computer to generate them. The quality of the Monte Carlo results depends largely on the capacity of the random number generator. A roulette wheel numbered zero to 36, can produce only 37 distinct random numbers. This program uses a Lagged Fibonacci pseudo-random number generator (http://csep1.phy.ornl.gov/rn/node20.html), considered to be one of the best. The Lagged Fibonacci generator is a 31-bit random number generator, providing $2^{31}$ ($\approx 10^9$) distinct random numbers. This provides sufficient capacity for a problem of this scope.

## 3.2 Implementation

A Fortran 90 computer code employing the Monte Carlo method is used to calculate IAM's for cylindrical solar collectors. The program operates by emitting a large number of photons from specified angles of incidence and tracing them until each is absorbed by one of the components of the collector's geometry. Each component can simply be thought of as a logical node for which a counter is incremented every time a photon is absorbed by it. The user supplies an input deck containing all the information the program needs to compute IAM's. This includes collector geometry, material specifications, a series of incident angles ($\theta_l$, $\theta_t$), a maximum number of photons to emit and a desired convergence tolerance ($C_{tol}$). The incident angles ($\theta_l$, $\theta_t$) constitute the rows and columns, respectively, of the matrix of IAM's. The angle of normal incidence ($\theta_l$=0, $\theta_t$=0) must be included, since IAM's are based on the collector's performance at normal incidence, as shown in eqn. (1.1).

### 3.2.1 Material Properties

The Monte Carlo method uses random numbers to determine the outcome when a photon intersects a surface. When a photon hits an opaque surface, a random number ($R_n$) is drawn to see if the photon is absorbed or reflected form the surface. The following conditional inequalities determine the outcome for the photon's interaction based on $R_n$:

$$R_n < \rho_d \quad \Rightarrow \quad \text{Diffuse Reflection} \tag{3.1}$$

$$\rho_d \le R_n < \rho_d + \rho_s \quad \Rightarrow \quad \text{Specular Reflection} \tag{3.2}$$

$$\rho_d + \rho_s \le R_n < \rho_d + \rho_s + \rho_{ss} \quad \Rightarrow \quad \text{Semi-specular Reflection} \tag{3.3}$$

$$\rho_d + \rho_s + \rho_{ss} \le R_n \quad \Rightarrow \quad \text{Absorbed} \tag{3.4}$$

If the photon is reflected diffusely or semi-specularly, a pair of random numbers ($R_n$, $R_{n+1}$) are used to determine the outgoing direction ($\theta_o$, $\phi_o$). For a diffuse reflection, the outgoing direction is distributed randomly about the surface normal. That is, using the first random number drawn, the outgoing azimuthal direction ($\phi_o$) is determined by the equation:

$$\phi_o = 2\pi \cdot R_n \tag{3.5}$$

The second random number determines the polar angle ($\theta_o$) based on equation 2.3:

$$\theta_o = \cos^{-1}\left( R_{n+1}^{\left(\frac{1}{1+r_d}\right)} \right) \tag{3.6}$$

recalling that $r_d$ is the parameter used to weight the directional distribution of diffuse reflections.

The semi-specular direction is chosen similarly, the difference being that the angles are randomly distributed about the specular reflection direction. Random numbers are not needed to determine the outgoing direction for a specular reflection, since its path is determined by the incident direction, as stated in eqn. (2.3).

When a photon intersects a glass cover from either side, the angle of incidence at which it strikes the glass is calculated. With this, the radiative properties of the glass ($\tau_g$, $\rho_g$, $\alpha_g$) are determined using the procedure outlined in section 2.3.2. A random number ($R_n$) is again used to determine if the photon is transmitted, reflected or absorbed, based on the glass' radiative properties at this angle of incidence. The following conditional inequalities determine the outcome based on the random number drawn ($R_n$):

$$R_n < \tau_g \quad \Rightarrow \quad \text{Transmitted} \tag{3.7}$$

$$\tau_g \le R_n < \tau_g + \rho_g \quad \Rightarrow \quad \text{Reflected Specularly} \tag{3.8}$$

$$\tau_g + \rho_g \leq R_n \quad \Rightarrow \quad \text{Absorbed} \tag{3.9}$$

Recall that transmissions occur without any displacement due to refraction, and reflections from the semi-transparent surfaces are always specular.

### 3.2.2 Ray Tracing Procedure

After reading the input deck, the computer program begins the Monte Carlo ray tracing procedure. The first angle of incidence (generally normal incidence) is chosen from which photons are emitted and traced (photon loops). The size and orientation of the emission plane is calculated to satisfy the current incident direction and to encompass the collector's surface completely with photon emissions. A user-specified number of photons, or block of photons, are emitted for every photon loop after which the optical calculations are made and convergence is checked. Photons are emitted from random locations ($x_e$, $y_e$, $z_e$) across the emission plane. These random locations are determined by using two random numbers. The first random number determines the distance along the bottom edge of the emission plane. The second random number determines the distance along the sides. For example, the random number pair (0.38, 0.57), establishes the location 38% across the width of the emission plane and 57% of the way up the emission plane. The photon is emitted with a path described by a unit vector normal to the emission plane's surface. The path of a line in three-space is described by the equation:

$$\frac{x - x_e}{e_x} = \frac{y - y_e}{e_y} = \frac{z - z_e}{e_z} \tag{3.10}$$

where $e_x$, $e_y$ and $e_z$ are the direction cosines of the photon's path along the x, y and z axes, respectively. The direction cosines for initial emissions are computed from the following three equations:

$$e_x = -\cos(\alpha) \cdot \cos(\phi) \tag{3.11}$$

$$e_y = \cos(\alpha) \cdot \sin(\phi) \tag{3.12}$$

$$e_z = -\sin(\alpha) \tag{3.13}$$

where $\alpha$ is the solar altitude and $\phi$ is the solar azimuth (east of $y = 0$ is positive).

Using eqn. (3.10) for the photon's path, intersection calculations are carried out to determine which surface the photon hits. It is first determined if the photon hits the aperture plane. If so, it is counted and used as a reference for the ($\tau\alpha$) calculation. This is done by simply intersecting eqn. (3.10) with the bottom plane ($z = 0$), and determining if the x and y values of the intersection point lie within the aperture plane. This is the only time the photon's path is intersected with the aperture plane.

Next, the photon's path is intersected with each of the glass cylinders. To aid in calculation efficiency, the intersection is first conducted in two dimensions (y-z plane). The equation of each cylinder in the y-z plane is simply the equation of a circle:

$$(y - y_0)^2 + (z - z_0)^2 = r_0^2 \tag{3.14}$$

recalling that ($y_0$, $z_0$) is the center of the circle, and $r_0$ the radius of the glass cover. Simultaneously solving eqn. (3.14) and the y-z components of eqn. (3.10) produces a pair of real solutions, ($y_{i,1}$,$z_{i,1}$) and ($y_{i,2}$,$z_{i,2}$), shown in Fig. 3.1, if the photon's path intersects the cylinder in these two dimensions. If the photon's path does not intersect the cylinder in these two dimensions, a complex solution results and the intersection calculations proceed for the next cylinder. Only one of the real solutions is valid. The first intersection point, shown as ($y_{i,1}$,$z_{i,1}$) in Fig. 3.1, is the valid one. This is determined by choosing the intersection point with the smallest positive change of the z component ($\delta z$):

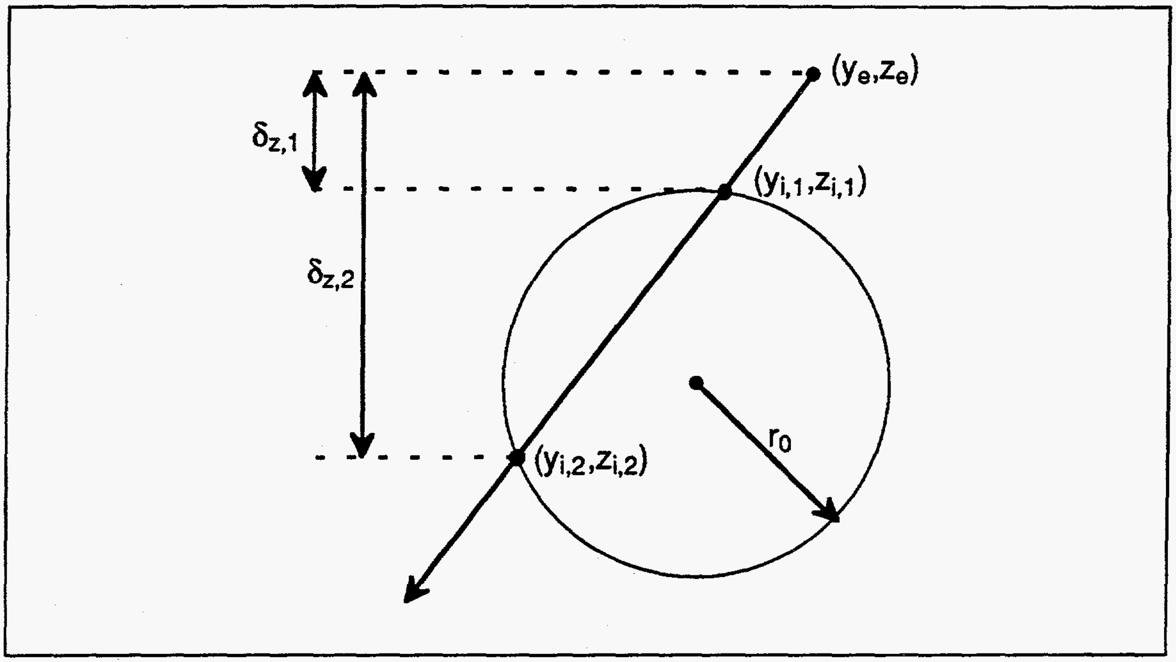

**Figure 3.1** Intersection of a Line with a Circle

$$\delta z = (z_i - z_e)e_z \tag{3.15}$$

Knowing the y and z values of the intersection point, eqn. (3.1) is used again to determine the x value of the intersection point in three dimensions. This intersection continues to be valid if it hits the cylinder within the x limits of the cylinder:

$$x_0 > x_i > x_0 - L \tag{3.16}$$

Each cylinder in front of the emission point must be checked to see if the photon hits it. The path will often intersect more than one cylinder. The valid intersection location ($x_i$, $y_i$, $z_i$) is stored each time the path intersects a cylinder. After all of the cylinders have been checked for an intersection, the intersection point of smallest δz determines the cylinder of intersection.

When a photon hits a glass cover, the outcome is determined by the procedure outlined in section 3.2.1. The following then occurs:

- If transmitted, the photon leaves from the intersection location without changing its direction and tracing continues to determine if the photon strikes the inner cylinder or the inner surface of the glass cover. Tracing continues inside the annulus until the photon exits the annulus or is absorbed.

- If reflected, the photon leaves from the intersection location in the direction of the specular reflection vector and the intersection calculations begin again.

- If absorbed, the absorption counter for the glass covers is incremented and a new photon is emitted.

If no cylinders are "hit," the photon's path is then intersected with the backplane. Similar to the intersection calculation with the aperture plane, eqn. (3.1) is intersected with the bottom plane ($z = 0$). If the x and y components of this intersection point lie within the limits of the backplane, the backplane is hit, and a new random number is drawn to determine if the photon is absorbed or reflected (subsection 3.2.1). If absorbed, the backplane absorption counter is incremented and a new photon is emitted from the emission plane. If reflected, a new direction is chosen based on the backplane material specifications, and tracing continues.

If the backplane is also missed, the photon is absorbed by the bottom plane, its absorption counter is incremented and a new photon is emitted from the emission plane.

A perfectly absorbing disk is automatically placed on both ends of every glass cylinder. This disk prevents photons from entering and exiting the end of the collector tube.

A photon hits this disk if the first intersection with the cylinder is beyond the extent of the collector tube in the x direction and the second intersection is within the extent of the collector tube in the x direction. The counter is incremented for the glass tube for the cylinder whose disk is intersected, and a new photon is emitted from the emission plane. A better method would involve the use of a planar surface placed over either end of the collector module to block photons from entering.

If a photon is not absorbed by any of the surfaces, the photon is considered lost. A lost photon implies an error in the code. A maximum number of lost photons is specified in the input deck. If this number is reached, execution of the program will stop and an error message will be displayed. To date, millions of photons can be traced without a single one being lost.

### 3.2.3 Convergence

The photon emission/ray tracing procedure continues until the user-specified number of photons for that photon loop have been emitted. After each photon loop completes, the current $(\tau\alpha)$ is calculated with eqn. (1.3), and the convergence factor [Maltby, 1990], C, is calculated:

$$C = \mathcal{Z}\sqrt{\frac{|1-(\tau\alpha)|}{(\tau\alpha)\cdot n_{ap}}} < C_{tol} \tag{3.17}$$

where $\mathcal{Z}$ is the cumulative normal distribution coefficient. The value of $\mathcal{Z}$ for 95% confidence is 1.96, taken from standard normal tables. Photon loops are executed either until $C < C_{tol}$, where $C_{tol}$ is the user supplied convergence tolerance, or until the user-specified maximum number of photon loops have been executed, after which the calculations proceed for the next angle of incidence.

## 3.3 Summary

With the completion of the calculations for all angles of incidence, the IAM's are calculated from eqn. (1.1). After that, a number of files are written. The file of interest is the matrix of IAM's (iam.tab). Table 3.1 shows an example of the file written in the format that TRNSYS requires. The first line specifies in degrees the longitudinal incidence angles, and the second line specifies the transverse incidence angles. Following that is the matrix of IAM's where the rows are for constant longitudinal incidence angles and the columns are for constant transverse incidence angles. Since a table of IAM's is useless without knowing the parameters of the collector for which the IAM's are calculated, the geometric and material parameters are summarized at the bottom of the file, and are not read by TRNSYS. The most important of these parameters are $(\tau\alpha)_n$ and the aperture plane area, as these are required values for the TRNSYS input deck.

**Table 3.1** Example of IAM's Output from Code, File iam.tab

| | | | | | | | |
|---|---|---|---|---|---|---|---|
| 0. | 40. | 80. | | | | | |
| 0. | 10. | 20. | 40. | 50. | 60. | 70. | 80. |
| 1.000 | 1.039 | 1.105 | 1.455 | 1.319 | 1.537 | 1.539 | 1.793 |
| 1.186 | 1.267 | 1.111 | 1.597 | 1.593 | 1.625 | 1.850 | 1.738 |
| 1.035 | 0.901 | 0.838 | 1.189 | 1.482 | 1.382 | 1.582 | 2.051 |

| | |
|---|---|
| $(\tau\alpha)_n$ | 0.5754 |
| $(\tau\alpha)_d$ | 0.7736 |
| $A_{ap}[m^2]$ | 2.4800 |
| $A_{bp}/A_{ap}$ | 1.1008 |
| $S_{bp}[m]$ | 0.1000 |
| $\rho_d$ | 0.0000 |
| $\rho_s$ | 0.8000 |
| $\rho_{ss}$ | 0.0000 |
| $r_{d,bp}$ | 0.0000 |
| $r_{ss,bp}$ | 0.0000 |
| $t_g{*}k_g$ | 0.0260 |
| $n_g$ | 1.5000 |
| $r_o$ | 6.3000 |
| $r_i$ | 5.5000 |
| L | 200.0 |
| $C_{tol}$ | 0.0100 |
| # of Direction s converged | 50 |

Tube Centers:

| | | | | | | | |
|---|---|---|---|---|---|---|---|
| -54.70 | -40.30 | -25.90 | -11.50 | 11.50 | 25.90 | 40.30 | 54.70 |

# CHAPTER 4 EXPERIMENTAL APPROACH

## 4.1 Introduction

A series of outdoor tests are conducted on a cylindrical solar collector. These tests are used to validate the IAM's produced by the new code. This chapter provides a detailed description of the collector module used in the outdoor tests and the geometric changes made to the collector. In addition the experimental procedures are outlined. These procedures include a heat gain test to verify the computed IAM's and a heat loss test to calculate an accurate overall heat loss coefficient ($UA_{coll}$). Finally, the data acquisition system and experimental error are described.

## 4.2 System Description

This section provides a detailed description of the collector module used in the experiments along with the variations made to the collector. The collector is mounted on the test bed (tilt = 45°, surface azimuth = 0°) at the Solar Energy Applications Laboratory (SEAL) at Colorado State University.

### 4.2.1 NEG Sun Family Collector

An NEG Sun Family collector is used for the experiments. This collector is a pair of four-tube integral collector-storage (ICS) modules connected in parallel. The total volume is 151 liters (40 gal). This is an evacuated tube collector, the space between the collector tube and the glass cover is evacuated ($P < 10^{-3}$ Pa) to minimize convective losses from the collector tube. Additional specifications for this collector are given in Table 4.1.

**Table 4.1** Specifications of NEG Sun Family Collector as Tested

| | |
|---|---|
| outside radius of glass cover ($r_o$) [m] | 0.063 |
| outside radius of collector tube ($r_i$) [m] | 0.055 |
| glass thickness ($t_g$) [m] | 0.002 |
| glass material | soda lime |
| absorber material | black chrome on copper |
| length of tubes (L) [m] | 1.99 |
| absorber area (projected) [$m^2$] | 1.75 |
| reflector area ($A_{bp}$) [$m^2$] | 2.60 |
| reflector material | polished stainless steel ($\rho_s = 0.6$) |
| manifold insulation | 1” pipe insulation |
| index of refraction for glass | 1.5 |
| extinction coefficient of glass [$m^{-1}$] | 0.15 |
| normal solar transmittance of glass | 0.90 |
| center pitch [m] | 0.22 |
| tube pitch (p) [m] | 0.152 |
| back plane to tube center spacing ($S_{bp}$) [m] | 0.08 |

Since this is a pair of four-tube modules, the pitch between the two center tubes (center pitch) is different than the standard pitch (p).

The manifold insulation given above is not that from the factory, which was a spray foam insulation (hole filler). Figure 4.1 shows the degradation of this insulation after exposing the empty collector to ambient conditions for a number of months. The degraded insulation was stripped from the manifold and replaced with 1” pipe insulation.

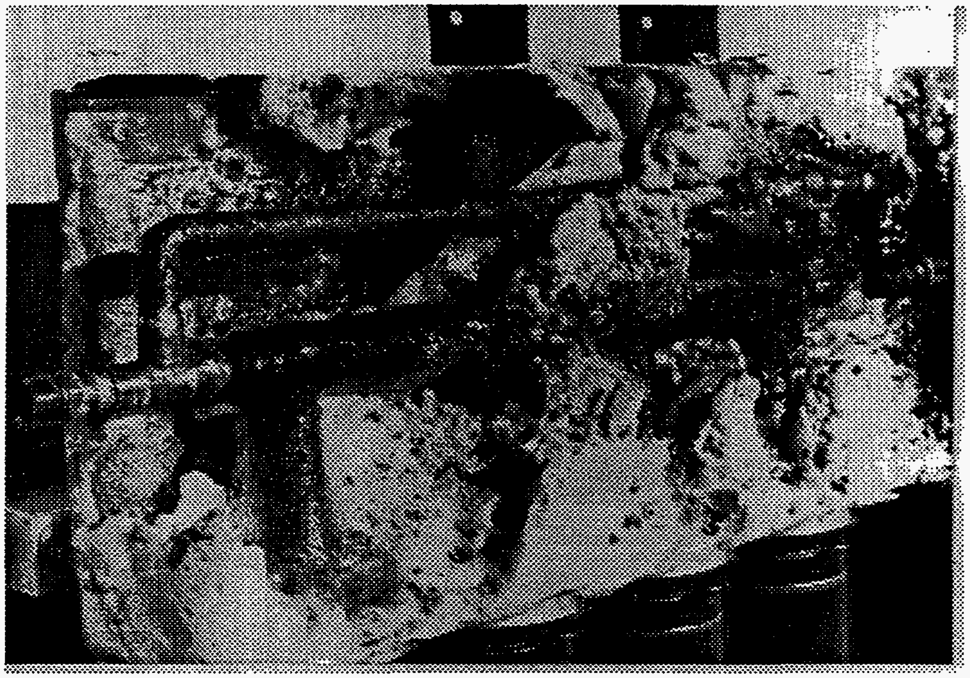

**Figure 4.1** Spray Foam Insulation Used in Manifold Cavity

### 4.2.2 Collector Variations

Changes were made to the shipped collector to provide a more robust validation. The two components of the collector's geometry easily amenable to change are the back plane reflectance and the tube pitch.

Four different back planes (parameters given in Table 4.2) are used during these tests to verify the back plane modeling. Three of the back planes, polished stainless steel, masonite painted white and masonite painted black, are mounted to the collector's frame approximately 0.08 m below the tube centers. The final back plane is the painted plywood surface of the test bed approximately 0.3 m below the tube centers.

Each of these back planes is used at two different tube pitches. The first tube pitch is that specified for the shipped collector in Table 4.1. Once all of the tests are conducted

**Table 4.2** Description of Various Back Planes Used in Experiments

| Back Plane Description | $\rho_d$ | $\rho_s$ | $\rho_{ss}$ | Dimensions (w x h) [m] |
|---|---|---|---|---|
| Polished Stainless Steel | 0.0 | 0.6 | 0.0 | 1.30 |
| Painted White Masonite | 0.7 | 0.0 | 0.0 | 1.68 |
| Painted Black Masonite | 0.1 | 0.0 | 0.0 | 1.68 |
| Test bed | 0.4 | 0.0 | 0.0 | 1.60 |

with this tube pitch, every other tube is removed from the module. This provides a standard pitch of 0.304 m and a center pitch of 0.372 m.

At least four days of data are collected for each back plane configuration and tube pitch. The days varied from partly sunny to very sunny.

## 4.3 Heat Gain Procedure

A heat gain procedure is used to measure the performance of the given collector configuration. Since this collector is an ICS module, it has sufficient capacitance ($mC_p$) so as not to require a forced flow during the test. However, on one occasion, a very clear day, the average temperature of the collector fluid did exceed the boiling point of water at 1 atm., thereby invalidating that particular test.

The tests consist of filling the collector with isothermal water in the morning, exposing it to ambient conditions for a portion of the day (typically 5-8 hours) and measuring the change in energy at the end of the test. Filling the collector with isothermal water was accomplished by drawing water through it until $T_{out} - T_{in} < 0.5°C$. The average initial temperature of the water in the collector ($\overline{T}_{initi}$) was taken to be $\frac{T_{out} + T_{in}}{2}$. Similarly, the energy in the collector at the end of the test is measured by drawing water through the collector until $T_{out}$ - $T_{in} < 0.5°C$. Typically this takes 4-5 tank volumes to accomplish. During this final draw, the inlet and outlet temperatures are measured along with the flow rate. The energy in the collector at the end of the test is calculated by:

$$E_{fin} = \int_t \dot{m} C_p \left(T_{out} - T_{in}\right) dt + E_{coll} \tag{4.1}$$

where $\dot{m}$ is the flow rate through the collector and $C_p$ is the specific heat of water and $E_{coll}$ is the energy left in the collector after the final draw:

$$E_{coll} = mC_p\left(\overline{T}_{end} - T_{ref}\right) \tag{4.2}$$

where $\overline{T}_{end}$ is the average temperature of the water in the collector after the final draw, taken to be the outlet temperature at the end of the final draw. The outlet temperature is representative of the average temperature because of the heat transfer in the manifold between the inlet and outlet streams. Several tests were completed using extended draws, whereby the final draw continued until ($T_{out}$ - $T_{in}$) < 0.1°C, essentially eliminating the energy left in the "tail" of the energy draw. This test was used to evaluate how closely the energy in the tank is measured by stopping the final draw when ($T_{out}$ - $T_{in}$) < 0.5°C. Using the outlet temperature as the final tank temperature provided the best results (within 0.5% of the final energy in the tank with the final $\Delta T$ during the extended draw less than 0.1°C).

An average temperature of the water at the end of the test ( $\overline{T}_{fin}$ ) can then be calculated by equating the energy drawn to that stored in the collector:

$$\overline{T}_{fin} = \frac{E_{fin}}{mC_p} + T_{ref} \tag{4.3}$$

where $mC_p$ is the thermal capacitance of the collector. This includes 151 kg of water and 20 kg of copper. The copper accounts for approximately 1.2% of the thermal capacitance of the collector. The thermal capacitance of the glass is neglected since its temperature does not change significantly with that of the water. The change in energy of the water for the test is then calculated from:

$$\Delta E = mC_p\left(\overline{T}_{fin} - \overline{T}_{initi}\right) \tag{4.4}$$

The collector is covered with an opaque tarp during the initial and final draws to minimize solar gains. Gains and losses are neglected during the final draw. With the temperature of the water in the collector dropping quickly and a low $UA_{coll}$, these losses amount to approximately 0.1% of the overall energy gain.

### 4.4 Heat Loss Test

A heat loss test is used to obtain an accurate $UA_{coll}$. The particular collector used for these tests is unique due to the insulation used on the manifold and, with the four tubes removed, the tube pitch. The pitch plays a significant factor in $UA_{coll}$ because of the increased amount of manifold per tube. As a result the $UA_{coll}$ was calculated for both the original eight tube module and the modified four tube module.

This procedure consists of filling the collector at dusk with hot, isothermal water, letting the collector sit uncovered overnight losing heat, and drawing off all the energy at dawn. Filling the collector with hot, isothermal water is achieved by exposing the collector to the sun during the day (or a number of days) to achieve a starting temperature of 60-80°C. A pump is then used to circulate water through the collector at a high flow rate (≈

0.5 l/s) until $T_{out}$ is approximately constant. The average temperature of the collector ($T_{ini}$) is then taken to be $T_{out}$. The same procedure used to measure the energy in the collector at the end of the heat gain test is used here to measure the energy in the collector at dawn. The use of eqn. (4.1) and eqn. (4.2) provides a final average temperature ($T_{fin}$):

$$T_{fin} = \frac{E_{fin}}{mC_p} + T_{ref} \tag{4.5}$$

The following equation governs the energy loss from a tank:

$$mC_p \frac{d\overline{T}}{dt} = UA\left(\overline{T} - T_{amb}\right) \tag{4.6}$$

where $\overline{T}$ is the average temperature of the fluid in the tank and $T_{amb}$ is the ambient temperature to which the tank is exposed. Integrating eqn. (4.6) using the simple Euler method and rearranging terms provides:

$$T_{n+1} = T_n - \left( UA \cdot \frac{T_n - T_{amb,n}}{mC_p} \right) \Delta t \tag{4.7}$$

where $T_n$ is the average temperature of the tank at the current time step, $T_{n+1}$ is the average temperature of the tank at the next time step, and $\Delta t$ is the number of seconds for each time step. Everything is known in this equation except $UA_{coll}$ and $T_{n+1}$. Guessing a value for the $UA_{coll}$ and integrating over all the time steps, the final average temperature ($T_{fin}$) can be calculated. A new $UA_{coll}$ is chosen until the calculated $T_{fin}$ is equal to the measured $T_{fin}$ (from eqn. (4.5)).

## 4.5 Data Collection

Figure 4.2 shows the system as it is installed on the test bed at SEAL. The instrumentation includes two Type-T thermocouples to measure collector inlet and outlet temperatures and one Type-T thermocouple housed in a vented radiation shield to measure ambient temperature. An EG&G Technologies turbine flow meter, connected to a frequency-to-voltage linearizer, is used to measure the flow rate through the collector. A pair of Eppley PSP radiometers are used to measure the solar radiation in the collector plane. One of these is fitted with a shadow band to measure the diffuse radiation in the collector plane. In addition to beam radiation, the shadow band also blocks part of the sky diffuse radiation. A corrective factor (from Eppley) based on the month of the year is used to correct the reading to within ± 2% of actual. Table 4.3 gives the shadow band corrective factors for average partly cloudy skies at 40°N latitude.

The data are collected using a digital data acquisition system consisting of an IBM compatible 386 computer with a Keithley MetraByte DAS-1602 I/O card installed inside the computer to read the voltage from the flow meter. An external Keithley MetraByte MTHERM-20 (12-bit A/D converter) thermocouple card is used to read the thermocouple and pyranometer output.

## 4.6 Experimental Error

Knowledge of the magnitude of the experimental error is necessary for interpreting the results of the experiment. The errors for individual measurements is obtained from the manufacturers specifications and calibrations, and are listed in Table 4.4.

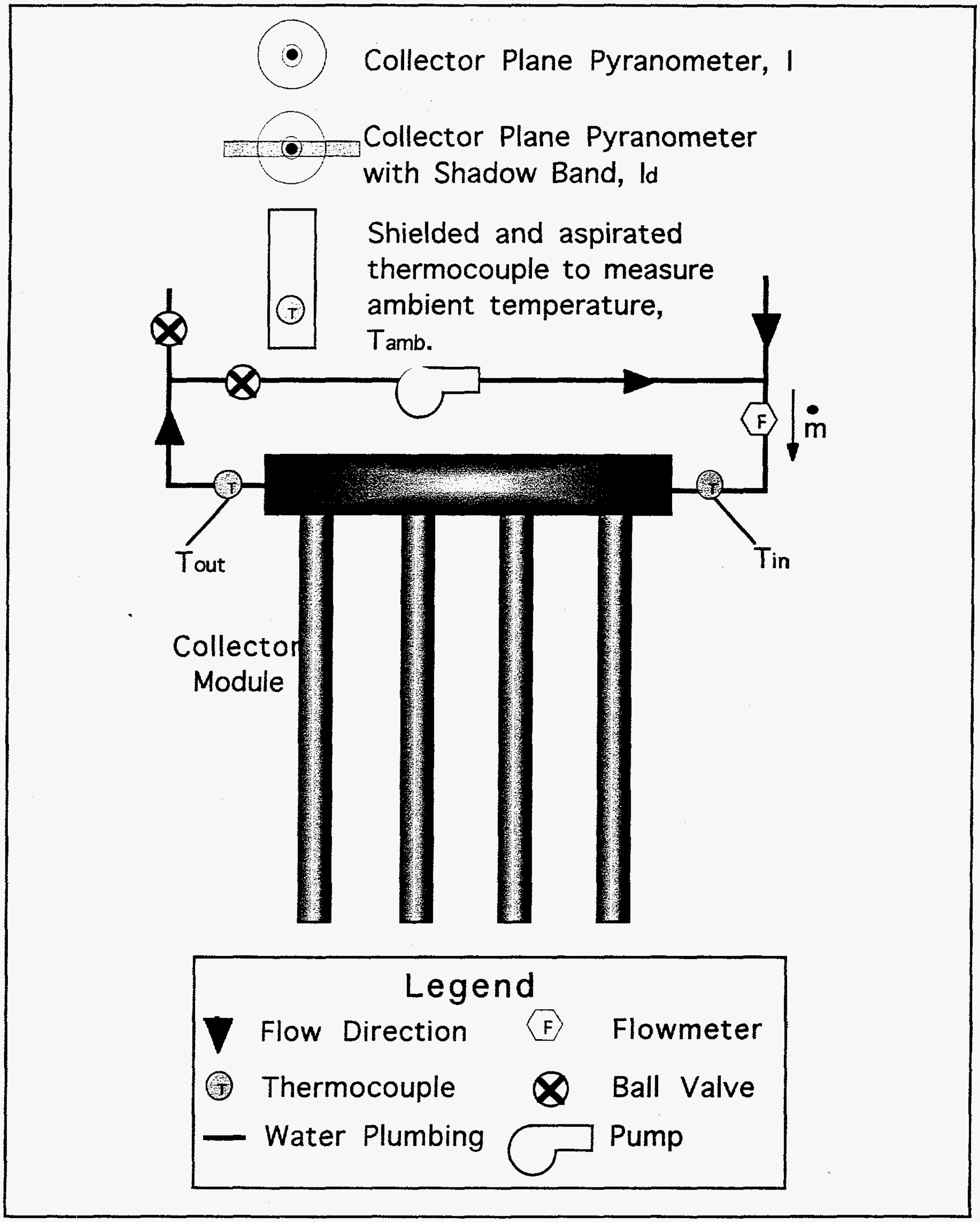

**Figure 4.2** System Instrumentation

**Table 4.3** Shadow Band Corrective Factors

| Jan. | Feb. | Mar. | Apr. | May | June | July | Aug. | Sep. | Oct. | Nov. | Dec. |
|---|---|---|---|---|---|---|---|---|---|---|---|
| 1.09 | 1.12 | 1.17 | 1.20 | 1.21 | 1.20 | 1.21 | 1.21 | 1.18 | 1.13 | 1.1 | 1.08 |

**Table 4.4** Uncertainty of Individual Measurements

| Measurement | Error |
|---|---|
| Type-T Thermocouple (calibrated) | ± 0.1°C |
| EG&G Turbine Flow Meter | ± 1% |
| Eppley PSP Radiometer | ± 2% |
| $UA_{coll}$ | ± 8% |

These errors are combined in quadrature to determine the error in a calculated quantity. That is, if ΔT is the temperature difference across the collector and is given by:

$$\Delta T = T_{out} - T_{in} \tag{4.8}$$

the error in calculating ΔT is found from:

$$\mathcal{E}_{\Delta T} = \sqrt{\left(\mathcal{E}_{T_{out}} \frac{\partial \Delta T}{\partial T_{out}}\right)^2 + \left(\mathcal{E}_{T_{in}} \frac{\partial \Delta T}{\partial T_{in}}\right)^2} \tag{4.9}$$

where $E_{\Delta T}$ is the error in measuring ΔT. Since each of the partial derivative terms reduce to an absolute value of one, $E_{\Delta T}$ reduces to:

$$\mathcal{E}_{\Delta T} = \sqrt{\mathcal{E}_{T_{out}}{}^2 + \mathcal{E}_{T_{in}}{}^2} \tag{4.10}$$

or

$$\mathcal{E}_{\Delta T} = 0.14\ ^\circ C \tag{4.11}$$

The experimental error, the error in measuring the amount of energy in the collector at the end of the test, is found by combining in quadrature the uncertainty in the equation:

$$q = \dot{m}C_p\Delta T\Delta t \tag{4.12}$$

where Δt is the time step. The error in Δt and the fluctuation of $C_p$ relative to temperature are considered negligible. The error in calculating the energy drawn off the tank is given by:

$$\mathcal{E}_q = \sqrt{\left(\mathcal{E}_{\dot{m}}\frac{\partial q}{\partial \dot{m}}\right)^2 + \left(\mathcal{E}_{\Delta T}\frac{\partial q}{\partial \Delta T}\right)^2} \tag{4.13}$$

Taking the partial derivatives and simplifying gives:

$$\mathcal{E}_q = C_p\Delta t\sqrt{\left(\mathcal{E}_{\dot{m}} \cdot \Delta T\right)^2 + \left(\mathcal{E}_{\Delta T} \cdot \dot{m}\right)^2} \tag{4.14}$$

Using representative values for an energy draw, summing over all the time steps of the draw and dividing by the drawn energy yields the relative error:

$$\mathcal{E}_{q,\%} = \frac{\mathcal{E}_q}{q} = \frac{822.3\ \text{kJ}}{39{,}938\ \text{kJ}} = 2.1\% \tag{4.15}$$

These errors vary slightly from one experiment to another, but are generally in the range of 2%.

Simulation error, the error in predicting the change in energy of the collector throughout the experiment, also exists. This error has four components:

- uncertainty in the radiation measurements (~2%)
- uncertainty in the ambient temperature measurement
- uncertainty in the overall heat loss coefficient, $UA_{coll}$
- errors in the TRNSYS and IAM models

The magnitude of the model errors is unknown and is neglected for the following analysis. The equation used by TRNSYS to determine the rate of change of energy of the collector is:

$$\dot{E} = A_{ap} \cdot (\tau\alpha)_n \cdot \left(IAM \cdot I_{beam} + IAM_d \cdot I_d\right) - UA_{coll} \cdot \left(\overline{T} - T_{amb}\right) \tag{4.16}$$

Combining the errors of the individual components in quadrature gives:

$$\mathcal{E}_{\dot{E}} = \sqrt{\left(\mathcal{E}_{I_{beam}} \frac{\partial \dot{E}}{\partial I_{beam}}\right)^2 + \left(\mathcal{E}_{I_d} \frac{\partial \dot{E}}{\partial I_d}\right)^2 + \left(\mathcal{E}_{UA_{coll}} \frac{\partial \dot{E}}{\partial UA_{coll}}\right)^2 + \left(\mathcal{E}_{\Delta T} \frac{\partial \dot{E}}{\partial \Delta T}\right)^2} \tag{4.17}$$

Taking the partial derivatives and simplifying gives:

$$\mathcal{E}_{\dot{E}} = \sqrt{\begin{array}{l}\left(\mathcal{E}_{I_{beam}} \cdot A_{ap} \cdot (\tau\alpha)_n \cdot IAM\right)^2 + \left(\mathcal{E}_d \cdot A_{ap} \cdot (\tau\alpha)_n \cdot IAM_d\right)^2 \\ + \left(\mathcal{E}_{UA_{coll}} \cdot \left(T_{amb} - \overline{T}\right)\right)^2 + \left(\mathcal{E}_{\Delta T} \cdot UA_{coll}\right)^2\end{array}} \tag{4.18}$$

Using representative values in the above equation and summing over all time steps, the relative error is:

$$\mathcal{E}_{\dot{E},\%} = \frac{\mathcal{E}_{\dot{E}}}{\dot{E}} = \frac{537.8 \text{ kJ}}{28{,}750 \text{ kJ}} = 1.9\% \tag{4.19}$$

Again, this error varies slightly from one experiment to the other, however it is consistently on the order of 2%. The error in the computer models has been neglected thus far. If the experimental error and the simulation error account for much of the difference between the experimentally measured energy and the predicted energy, that would imply the error in the models is small.

## 4.7 Summary

The experimental procedures have been kept simple to minimize the amount of inherent error. In addition to the results from the IAM code, the next chapter gives the results of the outdoor tests. Given an experimental error of 6%, and a simulation error of 2%, the experimental results and simulation results in general should be within 8% of each other. At this point, the procedure for testing a cylindrical solar collector has been defined and the next chapter will give the results of this test procedure.

# CHAPTER 5 RESULTS AND DISCUSSION

## 5.1 Introduction

The previous three chapters have described the theory and procedures used to model the performance of cylindrical solar collectors. This chapter provides the results of this study and uses these results to illustrate the effect of varying the collector geometry. This chapter starts with the verification of the computed IAM's. This includes both analytical and experimental results. In addition, a parametric study is used to illustrate the effect of varying the geometry and material properties of the collector. Once sufficient confidence in the computed IAM's exists, the collector design procedure commences.

## 5.2 Analytical Validation of IAM's

In this section, the code is verified using a specific case, for which the answers are known. Hundreds of particle traces with "real" material properties were output from the code and followed by hand. All checked exactly. However, on the order of 50,000 photons are emitted before 1% tolerance can be achieved for a single incident direction. Manually following every photon trace to verify the validity of a complete run would be prohibitively time consuming. There are some simple situations for which analytical solutions exist and can be tested. Consider a bank of black cylindrical solar collectors with a black ($\rho_{bp} = 0$) back plane and a transparent glazing ($\tau_g = 1.0$). At any angle of incidence for this collector, the value of $(\tau\alpha)$ should be equal to the ratio of the area of the cylinders projected into the emission plane to the area of the aperture plane projected into the emission plane. Using four collector tubes ($r_i = 0.055$ m, $L = 2.0$ m) with a pitch of 0.3 m, the calculations and results for $\theta_l = 0°$ and $\theta_t = 0°$ to 85° are given as Fig. 5.1. The curve is not smooth between 70° and 80°. At approximately 70°, inter-tube shading begins to occur, negatively affecting the performance. Beyond 75°, the performance curve quickly increases because the projected area of the aperture plane approaches zero, while the projected area of the cylinders approaches a constant value due to the height of the cylinders. The convergence tolerance for the IAM code is 1%, requiring approximately one million

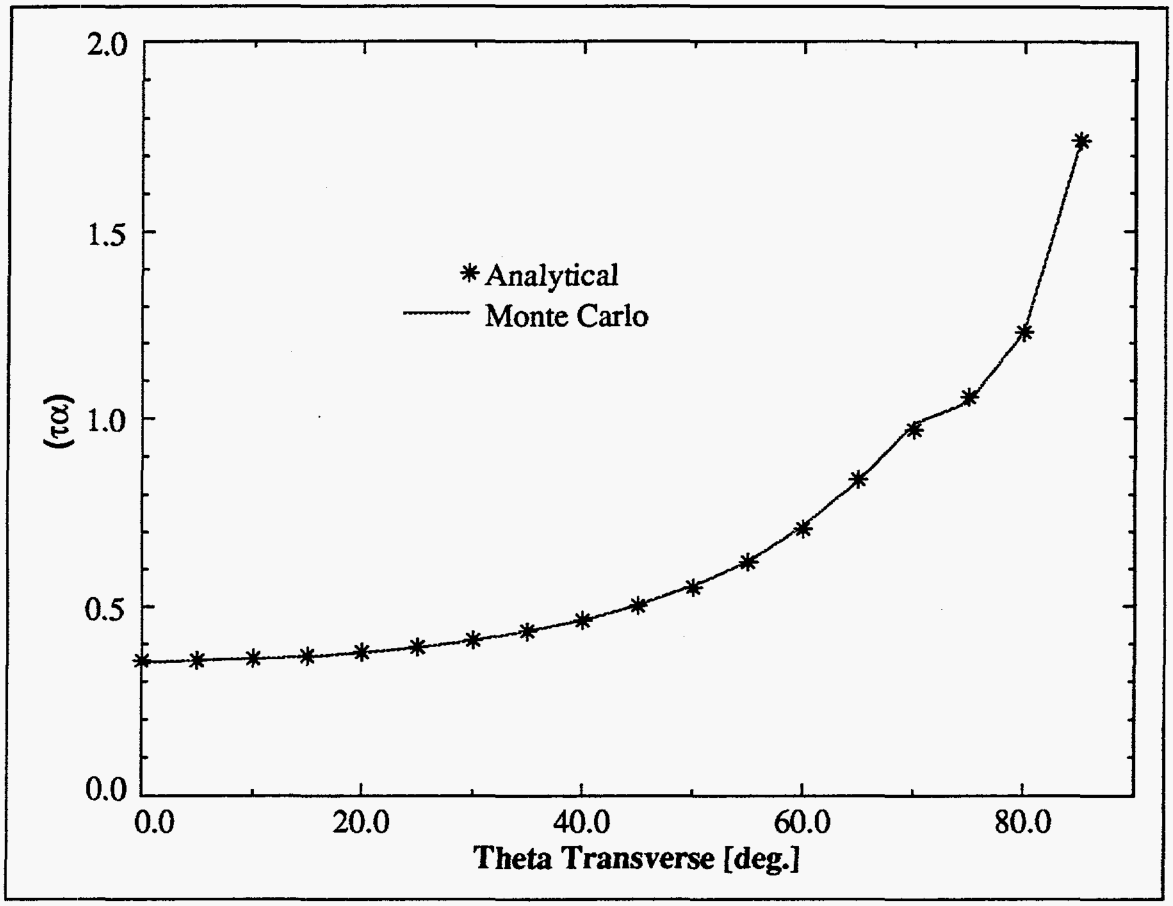

**Figure 5.1** Comparison of Analytical Results to Monte Carlo Results, $\theta_l$=0°

photon emissions for the eighteen incident directions. The average error for these 19 angles is 0.06% with a maximum error of 1.7%. This lends confidence that the photon tracing is correct.

## 5.3 Experimental Results

The results of the outdoor tests, the procedures for which are described in the previous chapter, are given here. First, the measured data are illustrated for a typical test. Figure 5.2 shows the radiation values collected on Sept. 28, 1996. This was a very clear day with a few clouds in the afternoon (between 2:00 P.M. and 3:00 P.M.). The "Tilt

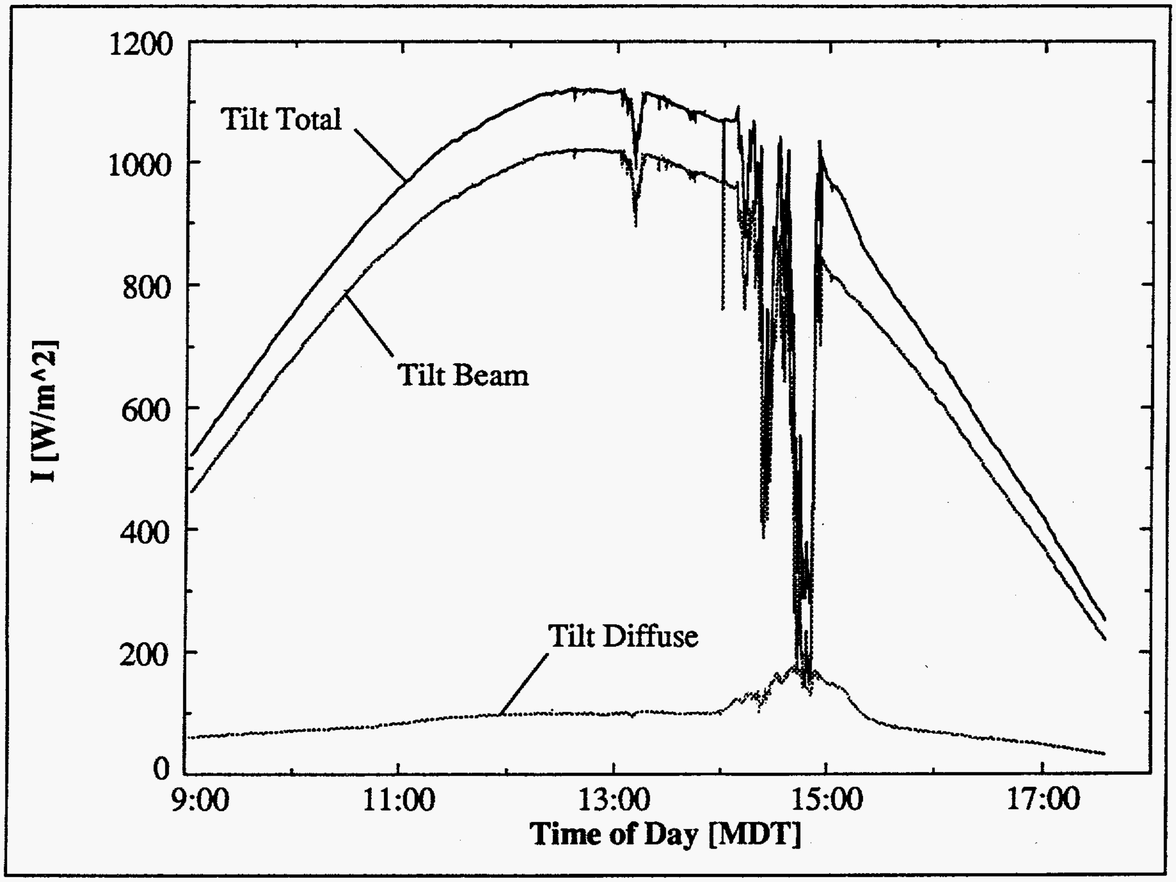

**Figure 5.2** Collector Plane Radiation on September 28, 1996.

Diffuse" value has been corrected for the shadow band, as explained in the previous chapter. The "Tilt Beam" value is calculated by:

$$I_{beam} = I - I_d \tag{5.1}$$

where I is the "Tilt Total" radiation component, measured directly.

Figure 5.3 shows the temperature measurements on this day. Notice the drop in temperature at the inlet and outlet to the collector ($T_{in}$, $T_{out}$) just before 3:00 P.M. This drop in temperature corresponds to the clouds in Fig. 5.2. These collector temperatures are for "no flow" conditions and are collected until just after 5:00 P.M. when the energy is drawn off via a purge. Notice the outlet temperature jumps up about 15°C at the beginning

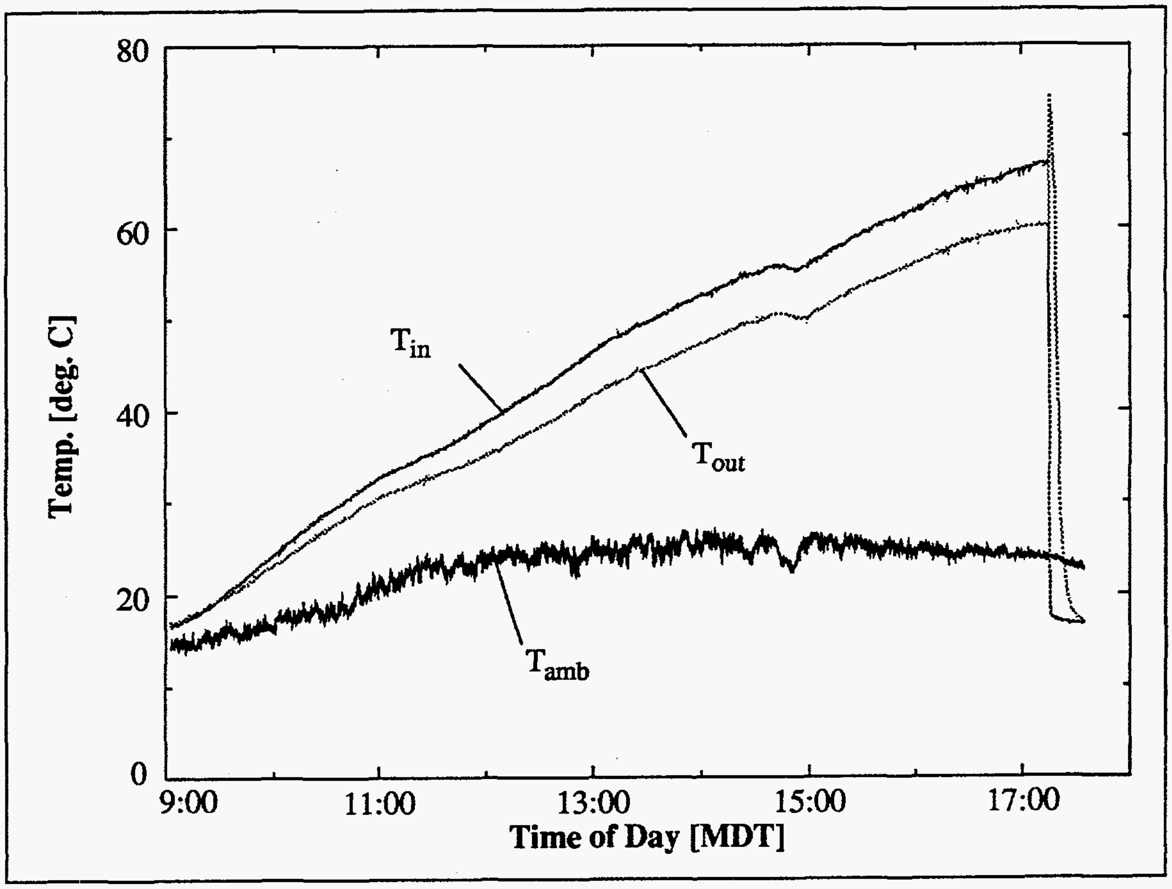

**Figure 5.3** Temperatures Measured on September 28, 1996

of the draw. This occurs because the temperature of the water in the collector is significantly higher than that at the outlet of the collector. Also, the ambient temperature ($T_{amb}$) varies more than the collector temperatures since the ambient thermocouple is in a low capacitance fluid: air.

### 5.3.1 Heat Loss Test Results

First the results from the heat loss tests are presented. The procedure for conducting these tests is described in the previous chapter. Table 5.1 summarizes these tests. In all, seven heat loss tests were performed. The first four of these were conducted on the collector when all eight tubes were still attached, while the last three were conducted on the collector with only four tubes attached. Significant variation exists in the measured $UA_{coll}$ for the eight tube tests, while the four tube tests exhibit less variation in the measured $UA_{coll}$. An average value for $UA_{coll}$ was taken for use in TRNSYS simulations:

**Table 5.1** Summary of Heat Loss Tests

| Date of Test | # of Tubes | Length of Test [hrs.] | $T_{amb,avg}$ [°C] | $T_{ini,avg}$ [°C] | $T_{fin,avg}$ [°C] | $UA_{coll}$ [W/°C] |
|---|---|---|---|---|---|---|
| 6/23/96 | 8 | 8.86 | 17.6 | 79.5 | 63.7 | 6.56 |
| 7/10/96 | 8 | 7.52 | 19.6 | 68.1 | 57.9 | 5.54 |
| 7/14/96 | 8 | 6.94 | 17.3 | 67.9 | 58.1 | 5.43 |
| 7/17/96 | 8 | 8.25 | 21.0 | 78.0 | 63.6 | 6.23 |
| 9/16/96 | 4 | 10.32 | 14.9 | 83.4 | 57.8 | 3.97 |
| 9/18/96 | 4 | 12.68 | 8.6 | 53.5 | 35.3 | 3.62 |
| 9/20/96 | 4 | 11.82 | 10.4 | 61.2 | 41.7 | 3.56 |

$$UA_{coll,8-tubes} = 5.9\frac{W}{^{\circ}C} \quad \pm 9\% \tag{5.2}$$

$$UA_{coll,4-tubes} = 3.7\frac{W}{^{\circ}C} \quad \pm 6\% \tag{5.3}$$

Equation (2.28) partitions the collector losses into tube losses and manifold losses. Assuming the losses from the manifold are the same for both the four tube collector and the eight tube collector, eqn. (5.2) and eqn. (5.3) can be used in conjunction with eqn. (2.28) to determine the loss coefficient for a single tube ($UA_{tube}$) and the loss coefficient for the manifold ($UA_{man}$). Solving the two equations for the two unknowns:

$$UA_{tube} = 0.55\frac{W}{^{\circ}C} \tag{5.4}$$

$$UA_{man} = 1.5\frac{W}{^{\circ}C} \tag{5.5}$$

Thus the manifold losses are approximately 25% of the overall losses for the eight tube collector module and approximately 40% of the losses for the four tube collector module. Knowing a loss coefficient per unit length of manifold will be useful for accurate annual simulations with a varying tube pitch. Dividing the manifold loss coefficient by the length of the manifold provides:

$$UA_{man,len} = 1.17\frac{W}{m{\cdot}^{\circ}C} \tag{5.6}$$

This assumes the manifold losses are a function of the length of the manifold, and not of the number of collector tubes attached to it.

### 5.3.2 Heat Gain Test Results

The heat gain test procedure was also described in the previous chapter. These tests are used to verify the computed IAM's for the various geometries of the collector. IAM's are computed for fifty different incident directions over a quarter of a hemisphere (assumes symmetry about the x and y axes) above the collector. Five longitudinal incident angles (0°, 20°, 40°, 60° and 80°) are combined with ten transverse incident angles (0°, 5°, 10°, 20°, 30°, 40°, 50°, 60°, 70° and 80°) to form a matrix and determine the fifty incident directions. The use of fifty incident directions provides a sufficiently fine mesh size, illustrated in Fig. 5.4. The IAM's and weather data are input to TRNSYS which in turn

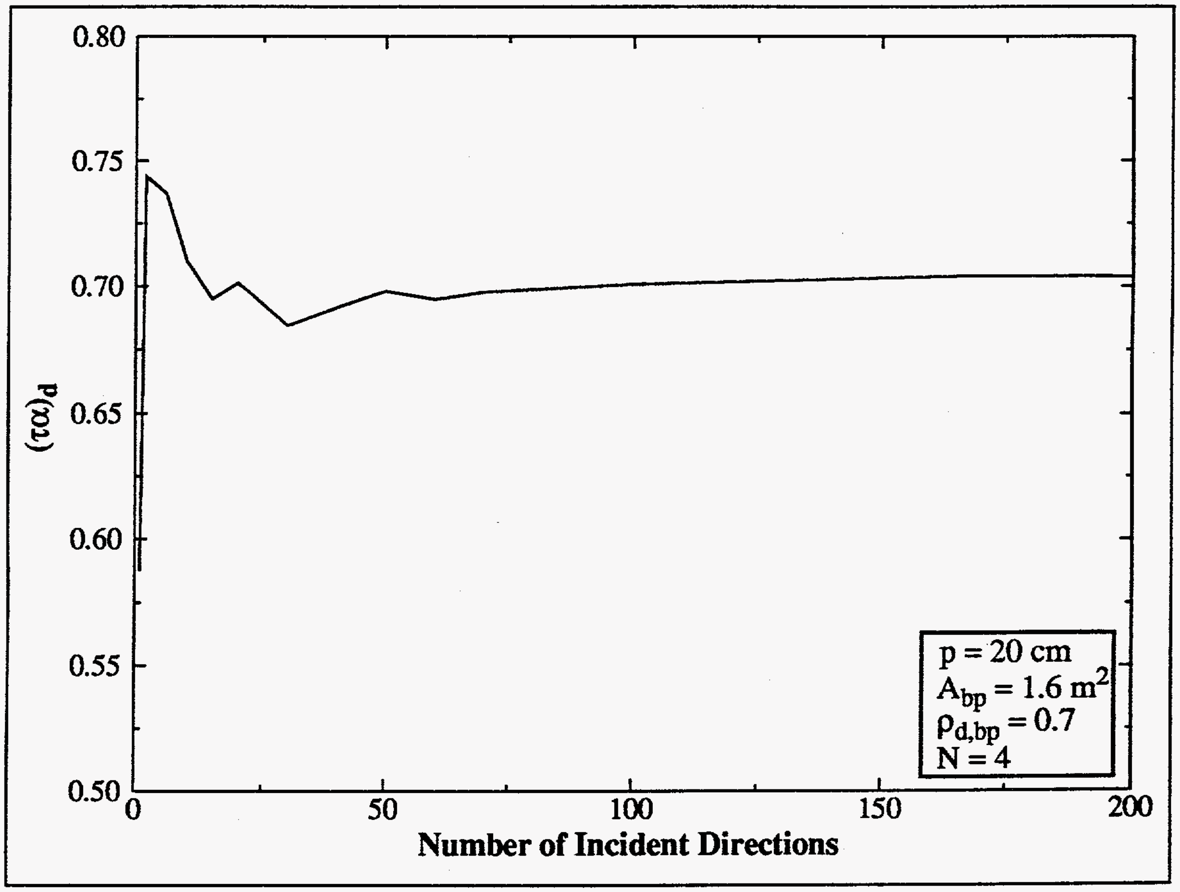

**Figure 5.4** Variation in $(\tau\alpha)_d$ with an Increasing Number of Incident Directions

predicts $\Delta E_{coll}$ for the experiment. Figure 5.5 shows the correspondence between the energy gain computed by TRNSYS and the measured energy gain. The average error for all the data points is 3.3%, with a maximum error for any single data point of 11.2%. The standard deviation of the errors is 5%.

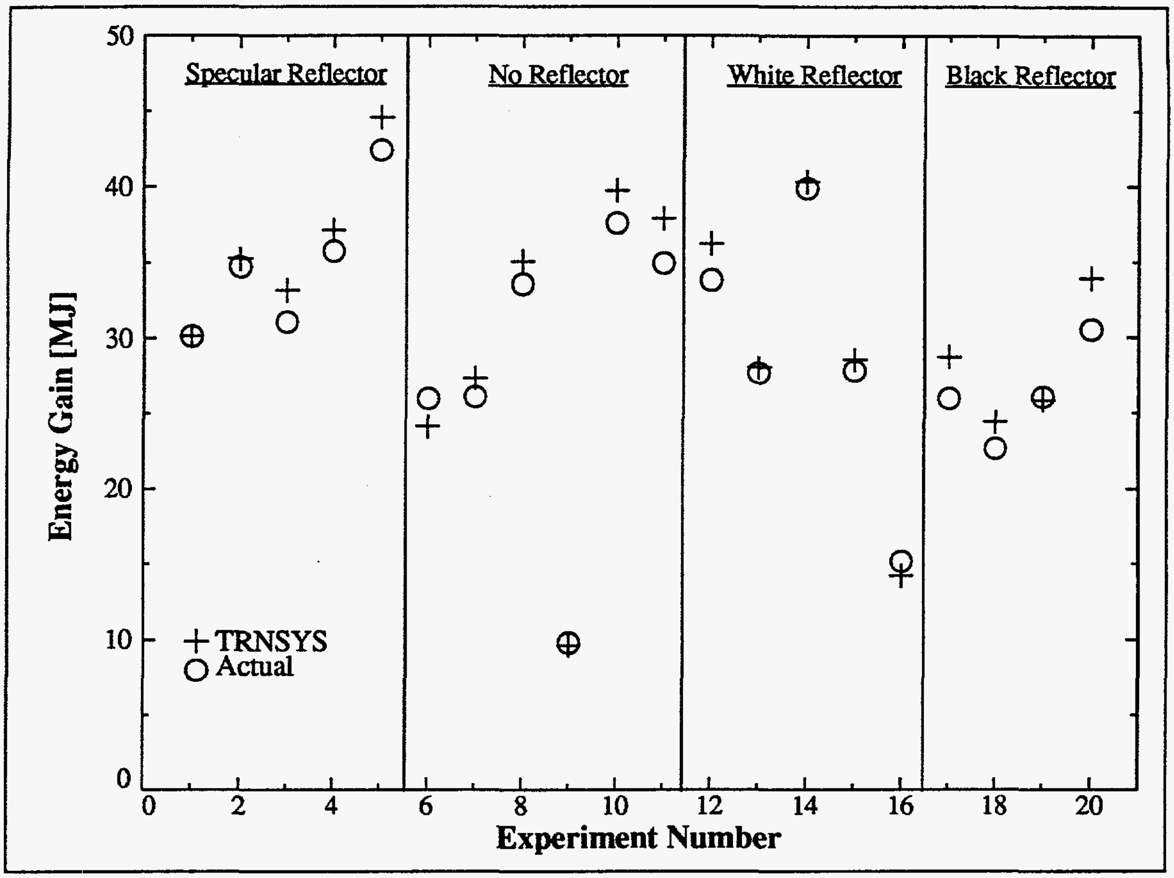

**Figure 5.5** Actual Energy Gain vs. TRNSYS Predicted Energy Gain, 8 Tubes

Similar tests were performed with this collector with four tubes removed. Figure 5.6 shows the correspondence between the actual energy gain of the collector and that computed by TRNSYS. Excellent agreement is also apparent for these tests. The maximum error is 8.6% with an average error of 1.3%. The standard deviation of theses errors is 3.8%.

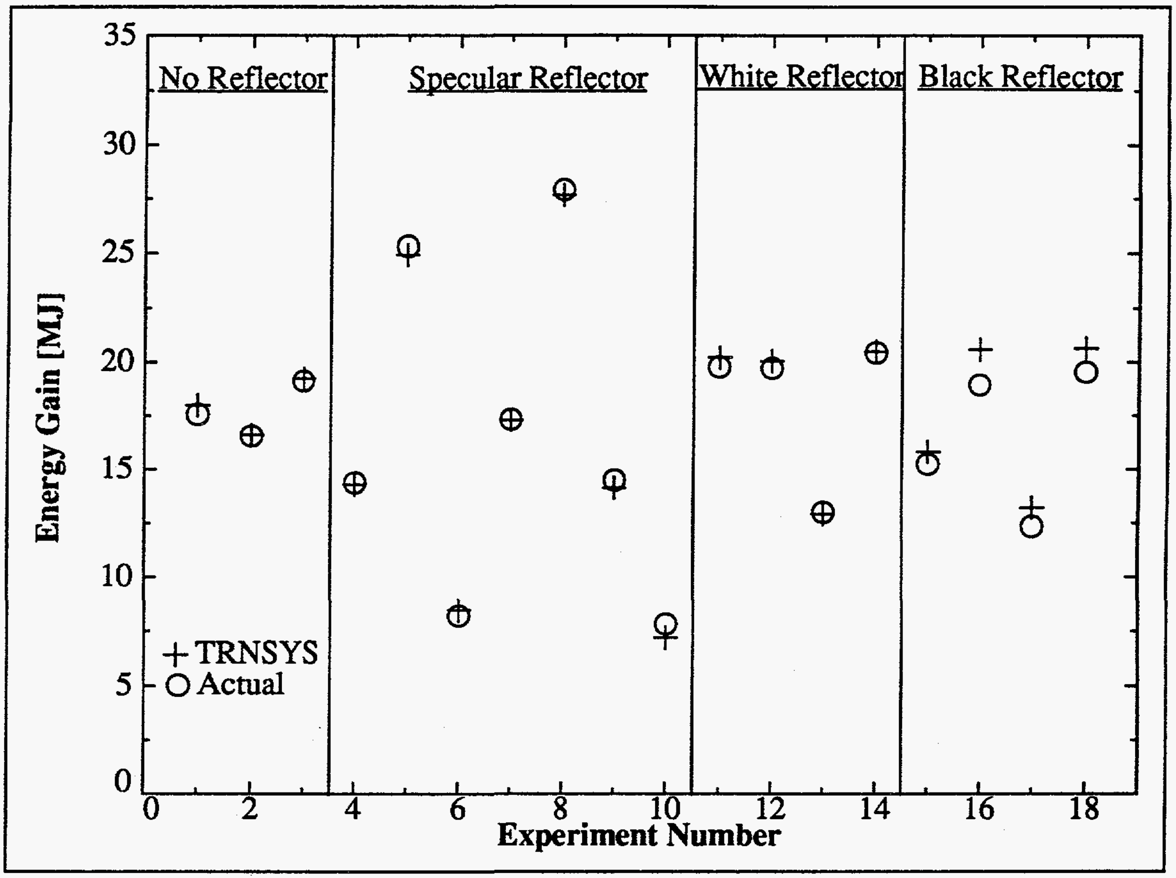

**Figure 5.6** Actual Energy Gain vs. TRNSYS Predicted Energy Gain, 4 Tubes

In the previous chapter, the experimental error and simulation error were each shown to be approximately 2%. Combining these in quadrature gives an overall error of 2.8%. The average difference between the simulated energy and the measured energy for the outdoor tests is expected to be in the general vicinity of the overall error. The average difference for all 38 tests is 3.8%. This implies the average error in the models is approximately 1%. With results as accurate as these, significant confidence exists in the validity of the computed IAM's.

General trends are apparent in the graphs in Fig. 5.5 and Fig. 5.6. The energy gain predicted by TRNSYS is typically higher than the measured energy gain. Certainly a study varying the material properties until a minimum error is obtained could be conducted.

However, a decision was made to use documented values for the material properties and examine the results. Clearly, these results are satisfactory based on the experimental error present.

### 5.4 Parametric Variation Results

A study of the effect on the IAM's of varying many of the collector components is illustrated in this section. This study is important for two reasons. First, the effect should be logical and justifiable. If this is the case, even more confidence can be placed in the computed IAM's. Second, a greater understanding of the significant parameters result, making the collector design procedure more efficient. Several methods can be used to illustrate the effect of varying the collector parameters. The most accurate method would be to compute the IAM's for each parameter variation and to run an annual TRNSYS simulation with these computed IAM's. Instead of taking the time to run so many annual TRNSYS simulations, an alternative method of comparison is used here. Here, the variation of the product of $(\tau\alpha)_d$ and $A_{ap}$, where $(\tau\alpha)_d$ is computed with eqn. (2.26) and $A_{ap}$ is computed with eqn. (2.1), is used as a performance metric. This represents the energy gain from diffuse radiation. The beam portion of the solar radiation is the significant component in predicting the performance of a solar collector. However, during an annual simulation beam radiation is incident upon the collector from much of the hemisphere above the collector. Since $(\tau\alpha)_d$ is the performance of the collector integrated over this hemisphere, it is believed that the product of $(\tau\alpha)_d$ and $A_{ap}$ will be a valid indicator of the performance for annual simulations. The correspondence between this and the annual energy gain is shown in Fig. 5.7, for four geometries. Although the values are of different orders

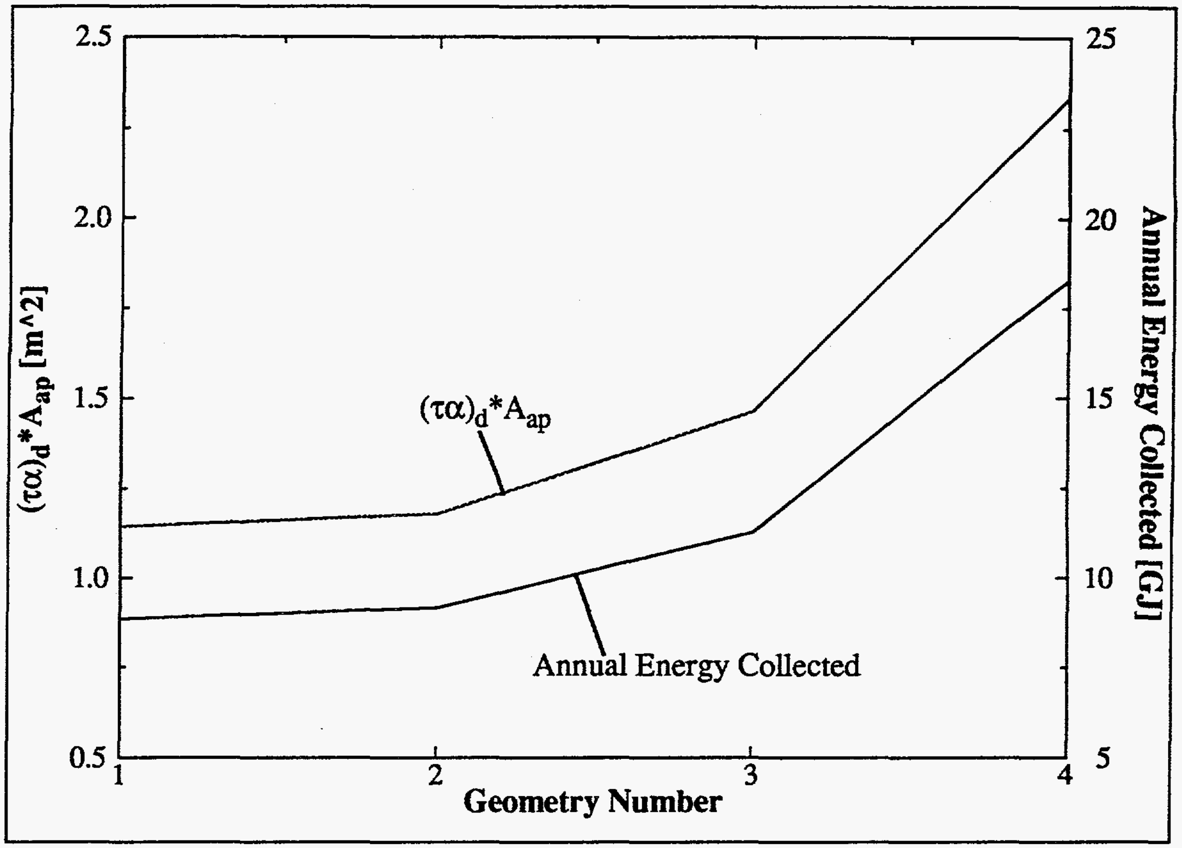

**Figure 5.7** Comparison of Annual Energy Collected vs. $(\tau\alpha)_d*A_{ap}$

of magnitude the correspondence is clear. The significant parameters for these four geometries are given in Table 5.2. The tubes used for this illustration are identical to the collector tubes described in Table 4.1, the shipped collector tubes.

The following subsections illustrate the effect of varying the collector parameters. In all of these subsections, four collector tubes, with the same characteristics as the tubes tested, are used unless stated otherwise. All diffuse surfaces are modeled using a diffuse weighting exponent ($r_d$) of 1.0, and all semi-specular surfaces are modeled using a semi-specular weighting exponent ($r_{ss}$) of 2.0.

### 5.4.1 Effect of Tube Pitch

In this section, the effect of varying the tube pitch is illustrated. Eight tube pitches are used to accomplish this. Figure 5.8 shows the effect of varying the tube pitch. Four

**Table 5.2** Significant Parameters for Geometries in Fig. 5.7

| | Geometry 1 | Geometry 2 | Geometry 3 | Geometry 4 |
|---|---|---|---|---|
| Pitch [m] | 0.20 | 0.20 | 0.40 | 0.20 |
| Number of Tubes | 4 | 4 | 4 | 8 |
| $\rho_{s,bp}$ | 0.6 | 0.0 | 0.0 | 0.0 |
| $\rho_{d,bp}$ | 0.0 | 0.8 | 0.9 | 0.9 |
| $r_{d,bp}$ | 0.0 | 0.0 | 1.0 | 1.0 |
| $A_{bp}$ [$m^2$] | 1.89 | 1.89 | 3.57 | 3.57 |
| $A_{ap}$ [$m^2$] | 1.60 | 1.60 | 3.20 | 3.20 |

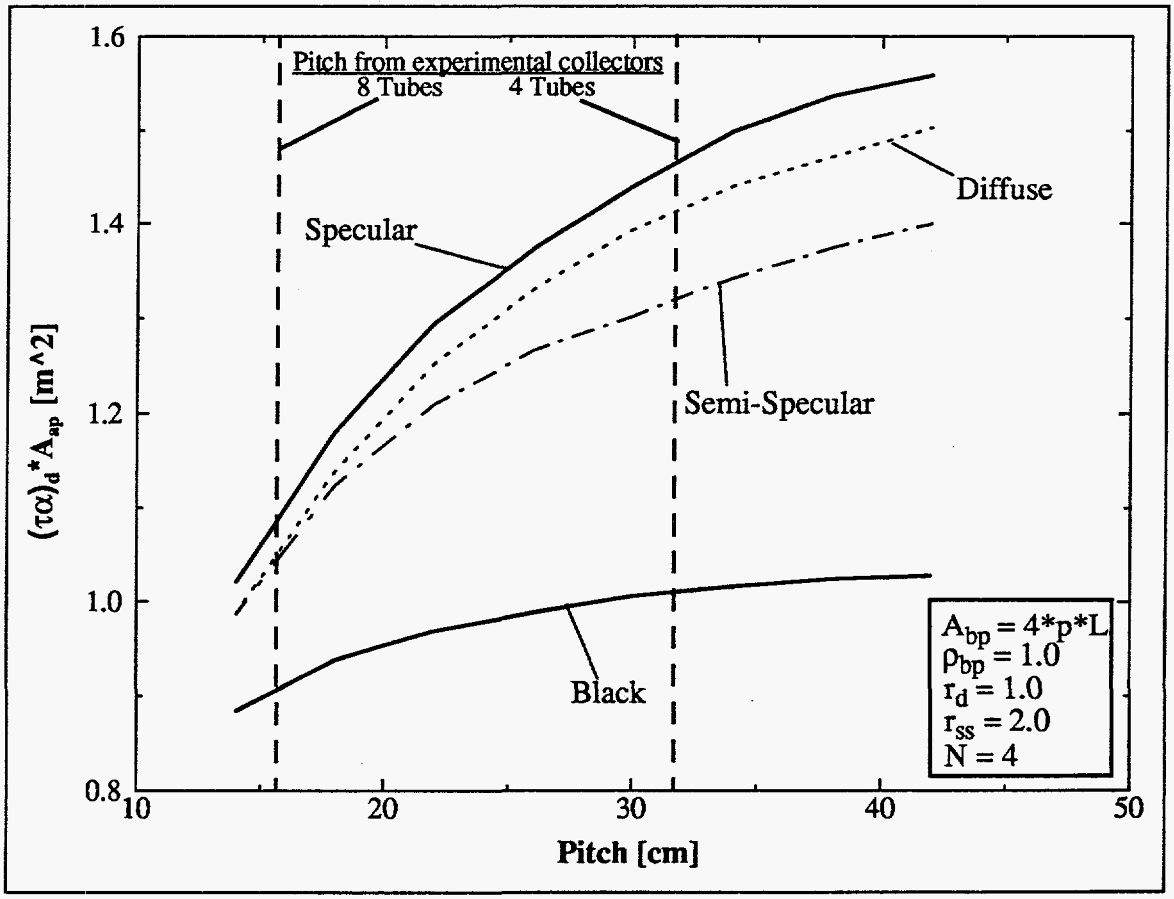

**Figure 5.8** Effect of Increasing the Tube Pitch

back planes are used to distinguish the effect of inter-tube shading from the effect of radiation passing between the tubes and reflecting back at the tubes. The first is a perfectly absorbing ($\rho_{bp}$ = 0.0) back plane to illustrate simply the effect of inter-tube shading. The other three are perfectly reflecting specular, diffuse and semi-specular back planes. These illustrate both the effect of inter-tube shading and the effect of radiation reflected from the back plane. Here the size of the back plane is equal to the size of the aperture plane, eqn. (2.1). A value of 14 cm is used as the smallest pitch, and the pitch is increased 4 cm at a time to a maximum value of 42 cm.

It is clear from Fig. 5.8 that the effect of inter-tube shading is much less significant than the effect of radiation passing through the tubes and reflecting from the back plane back to the tubes. Although the performance of the collector with the black back plane does increase with increasing pitch, the increase is significantly smaller than the increase for the reflective back planes. The performance of the collectors with reflective back planes increases significantly until a tube pitch of approximately 30 cm, at which point the performance curves begin to flatten.

It is expected that these curves approach an asymptotic value. This maximum is characterized by the performance of a single tube above an infinite white backplane. The code was run for a single tube above a large (140 cm x 210 cm), white back plane. Multiplying this $(\tau\alpha)_d$ by the aperture area and then by four (the number of tubes), yields an asymptotic value of 1.63 $m^2$.

### 5.4.2 Effect of Back Plane Reflectance

Figure 5.8 illustrates how significant is the use of a back plane reflector. This subsection illustrates the effect of varying the back plane reflectance. Three different tube pitches (14 cm, 20 cm and 30 cm) are used in Figure 5.9. A linear relationship is evident between the reflectance of the backplane and the performance of the collector. A linear relationship is expected, in that increasing the reflectance of the back plane linearly increases the number of photons leaving the back plane, thus increasing the number of photons incident upon the collector. The slope of the performance curves increases with a larger pitch, implying the advantage of using both an increased pitch and a reflective back plane. Again, the effect of using a back plane reflector is significant, with an increase in performance of between 23% and 30% depending on the type of reflector used and the pitch.

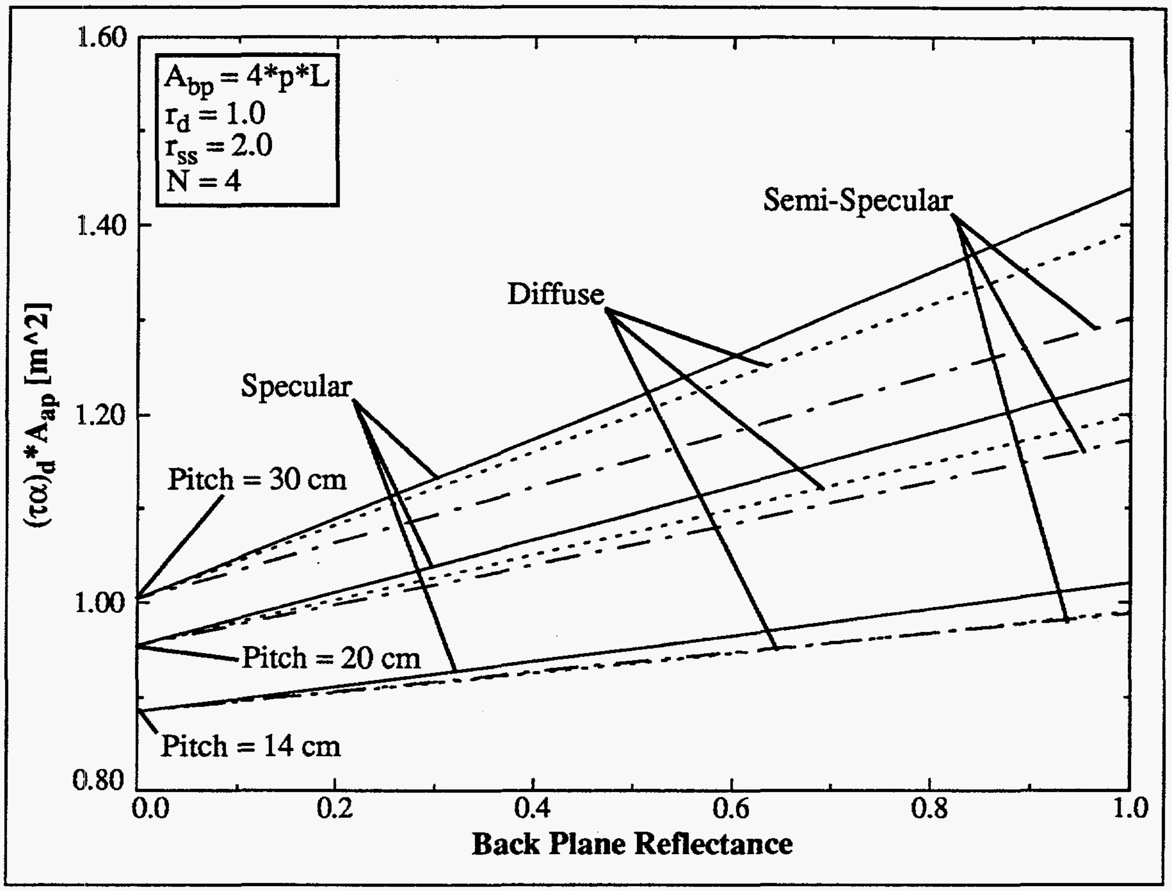

**Figure 5.9** Effect of Back Plane Reflectance with Three Pitches

### 5.4.3 Effect of Back Plane Width

Increasing the width of the back plane beyond the extent of the collector tubes increases the amount of radiation incident upon the collector. The effect of this increased width on the collector's performance is illustrated in Fig. 5.10, for three different back plane reflectors. These are perfectly reflecting specular, diffuse and semi-specular back plane reflectors. Five backplane widths are used. The smallest width (80 cm) is the width of the aperture plane or the number of tubes multiplied by the pitch. Similar to the previous section, a pitch of 20 cm with the four collector tubes is modeled. The greatest

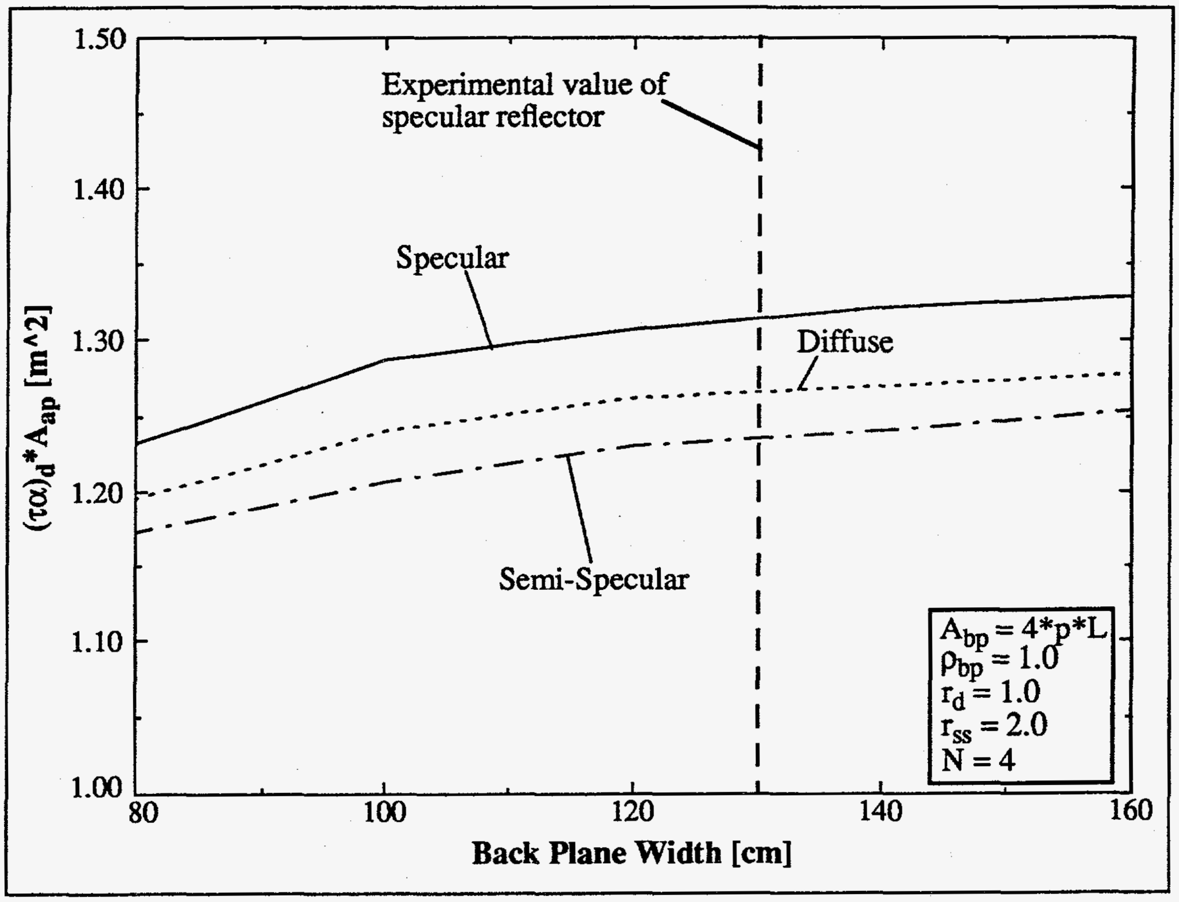

**Figure 5.10** Effect of Increasing the Back Plane Width

increase in the collector's performance is for small increases in the back plane width, however this increase quickly diminishes beyond a width of 100 cm.

### 5.4.4 Effect of Back Plane to Tube Spacing

The effect of increasing the back plane to tube spacing is now analyzed. Figure 5.11 shows the effect of increasing the back plane to tube spacing. Once again three, perfectly reflecting back planes are used to produce this figure. Five back plane to tube center distances are used: 8, 12, 16, 20 and 24 cm. With the glass cylinders having an outside radius of 6.3 cm, the smallest value of 8 cm (approximately the same as that of the unit tested) places the back plane very close to the glass tube. Optimum performance for all

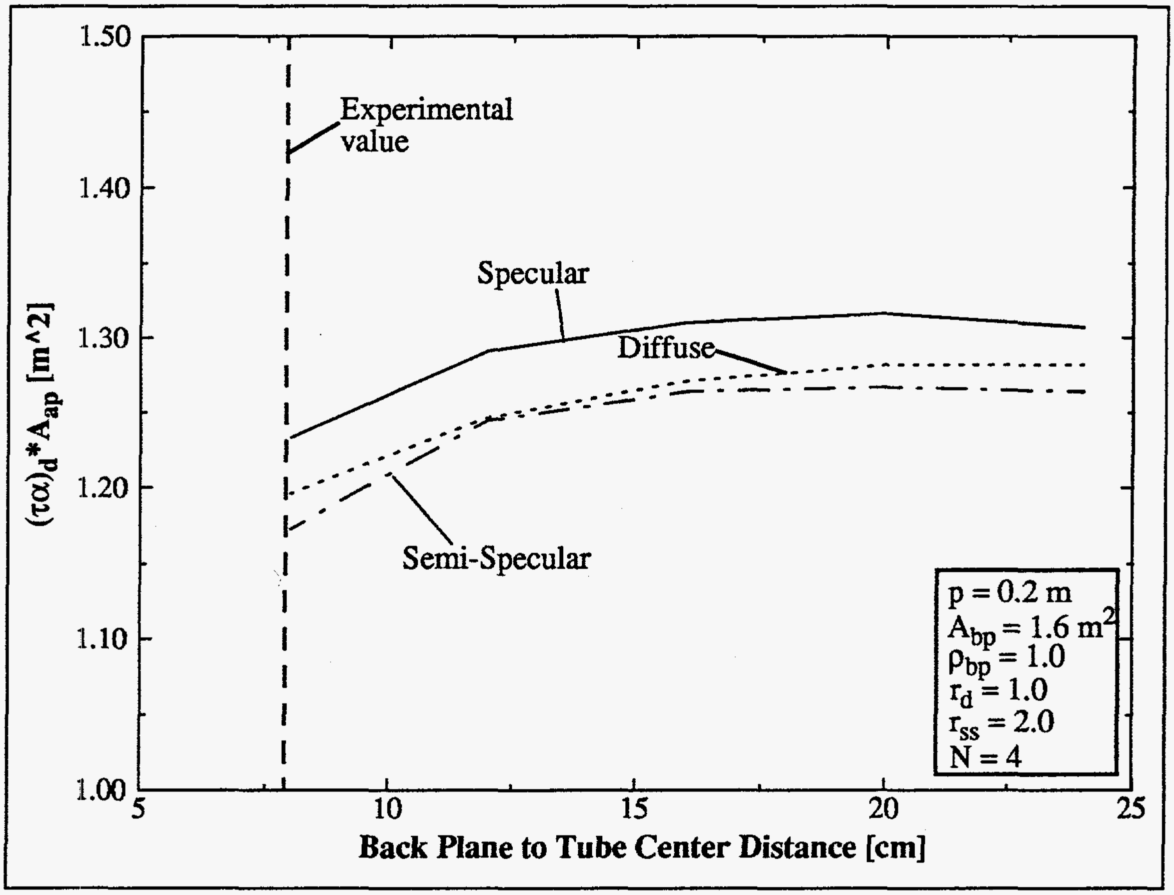

**Figure 5.11** Effect of Increasing the Back Plane to Tube Center Distance

three back planes occurs around a value of 20 cm, after which the performance actually declines for the specular and semi-specular reflectors. The increase in the performance is reasonable because as the collector tubes are placed further from the back plane, more radiation will hit the back plane at off-normal incident directions. However, as this distance continues to increase, the view factor from the tubes to the back plane decreases, thus causing the performance curve to achieve a maximum and eventually decrease.

Although an optimum value occurs around 20 cm, structural, packaging and mounting problems may occur with the collector so far away from the reflector. A better value may be around 12 cm.

### 5.4.5 Effect of Collector Tube Absorptance

The absorptance of the collector tube is quite significant for obvious reasons. Solar collectors have dark absorbers to absorb as much of the incident radiation as possible. Figure 5.12 illustrates the effect of varying the collector tube absorptance. A four tube collector is placed above a perfectly reflecting specular reflector. Once again a linear relationship is apparent. Of the photons which intersect the collector tube, a portion will be absorbed based on the absorptance of the tube. Varying this absorptance should generate a linear response in the collector's performance.

### 5.4.6 Effect of Glass Properties

The final parametric study involves the glass properties and their impact on the performance of the collector. Figure 5.13 illustrates the effect of varying the index of refraction ($n_g$) for the glass covers. The glass fraction is the ratio of the number of photons absorbed by the glass to the number of photons emitted. Again the collector is mounted above a perfectly reflecting specular reflector. Examining the semi-transparent surface

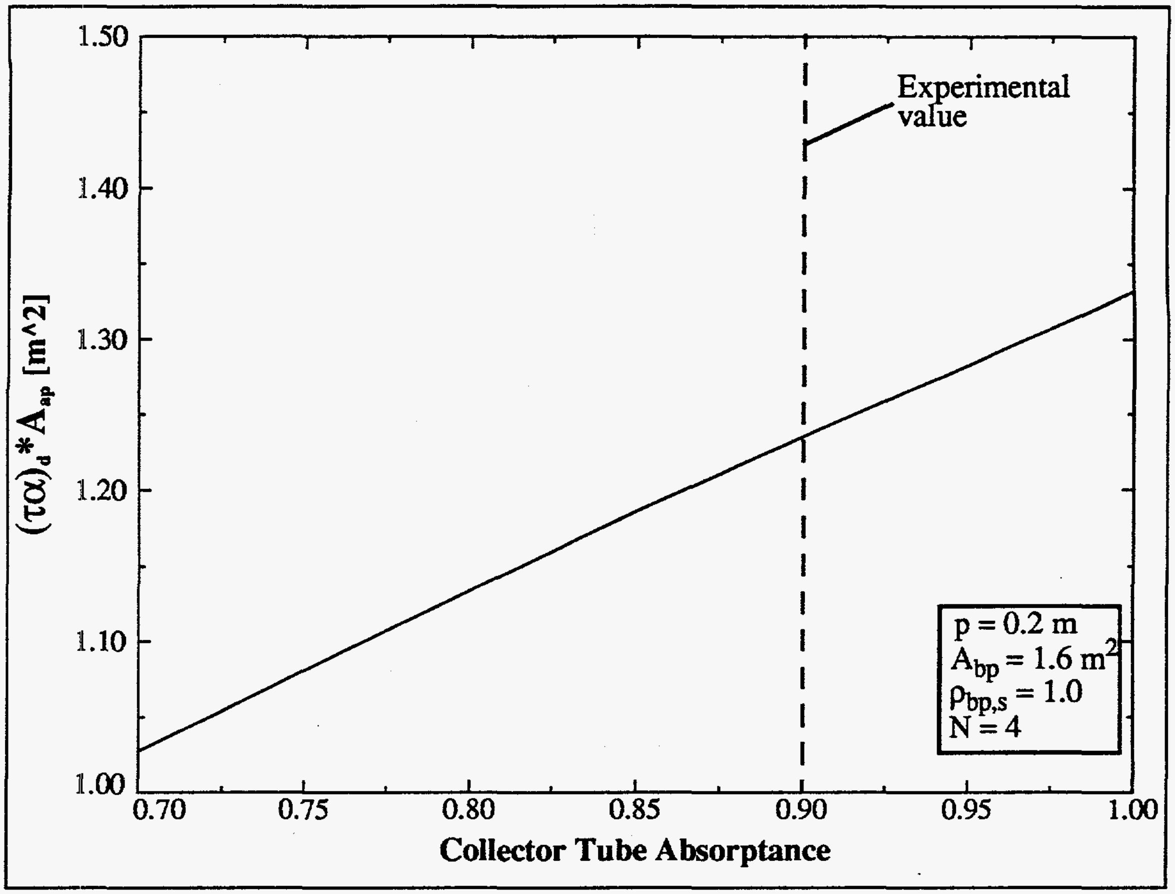

**Figure 5.12** Effect of Varying the Collector Tube Absorptance

equations in chapter 2 explains the curves in Fig. 5.13. The index of refraction of the glass has more to do with the reflectance of the glass' outer surface than the glass' absorptance. The angle of refraction increases with smaller indices of refraction, causing greater absorption due to a greater path length (eqn. (2.13)). However this is not the dominating feature illustrated in Fig. 5.13. The glass fraction slightly decreases with increased indices of refraction. More photons are reflected from the glass' surface due to eqn. (2.11) and eqn. (2.12), hence fewer photons enter the glass. This is the reason for a decreasing collector performance with an increase in the index of refraction

The glass thickness ($t_g$) and extinction coefficient ($k_g$) are also varied to evaluate their impact on the collector's performance. These two parameters are varied as a single

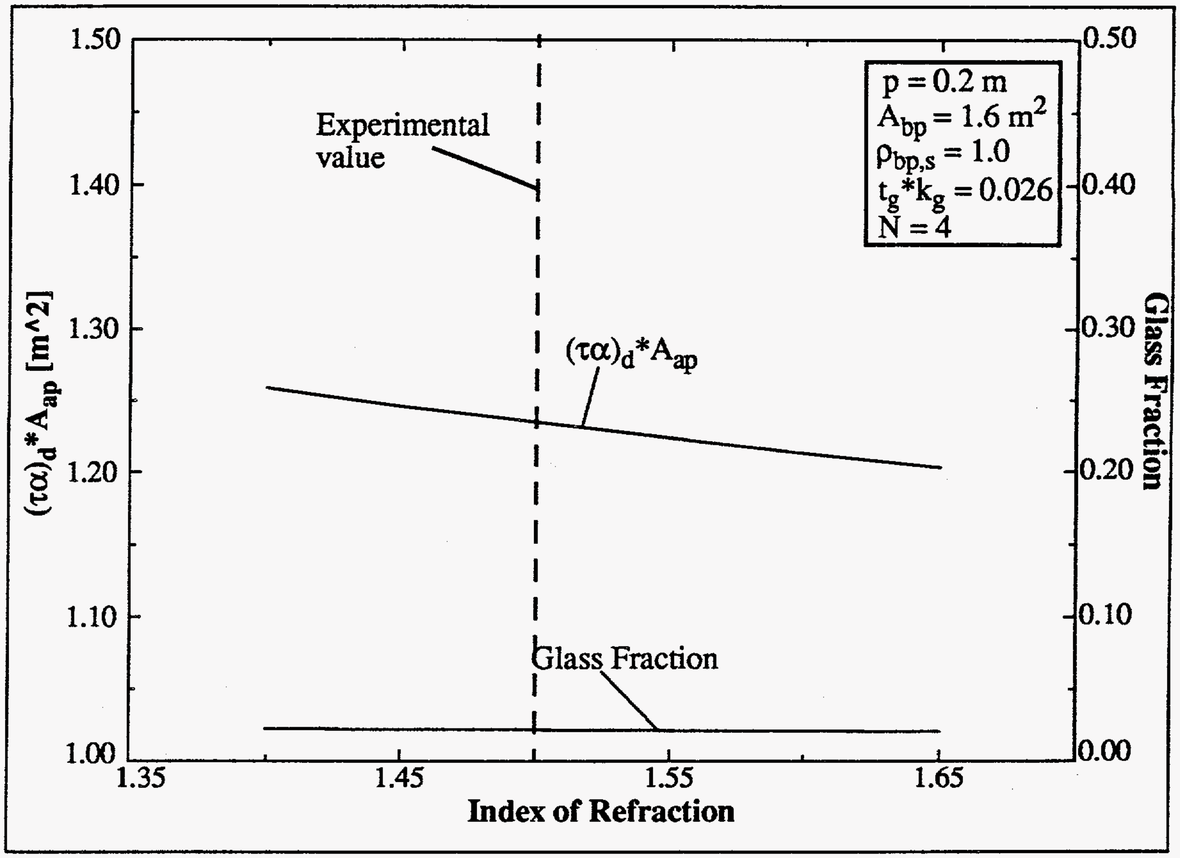

**Figure 5.13** Effect of Varying the Index of Refraction of the Glass Covers

product, as they show up in the semi-transparent surface equations in tandem. Also, their product is dimensionless. Figure 5.14 illustrates the effect of varying the product these two parameters. Again the performance varies linearly with the product ($t_g{*}k_g$). Unlike for a larger index of refraction, the degradation in the collector's performance here is primarily due to increased absorptance in the glass. This is apparent in the increasing glass fraction as $t_g{*}k_g$ increases. Clearly this should be the case. Whether the thickness of the glass is increased or the extinction coefficient is increased, a greater number of photons should be absorbed by the glass (eqn. (2.13)).

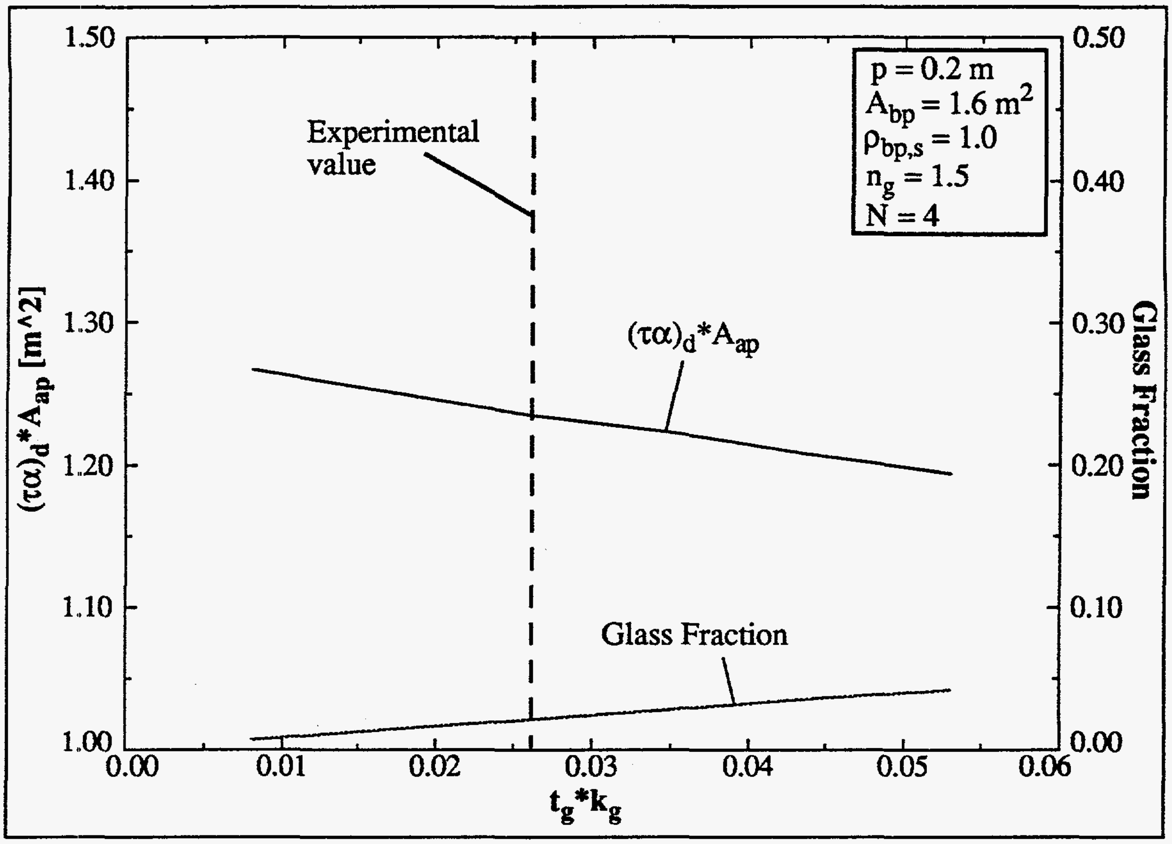

**Figure 5.14** Effect of Varying the Thickness of the glass ($t_g$) and Extinction Coefficient ($k_g$)

## 5.5 Cylindrical Solar Collector Analysis

The previous section illustrates the effect of varying many of the design parameters for a cylindrical solar collector. Increasing the tube pitch along with the use of a back plane reflector significantly enhances the collector's performance (Fig. 5.8), while extending the width of the back plane beyond the extent of the collector's aperture plane has much less influence (Fig. 5.10). This section uses the insight gained from the previous section to perform an analysis of the effect on annual performance of varying some design parameters. For simplicity this study is limited to the use of four collector tubes, however the results of this study should be transferable to a collector with more tubes. Not all of the collector's components are easily changed in real life. As a result only reasonable variations are considered here:

- tube pitch
- back plane reflectance
- back plane width

The tube pitch is varied from a minimum of 14 cm to a maximum of 30 cm. Figure 5.8 suggests a tube pitch larger than 30 cm provides only a small performance increase. In addition, extending the back plane significantly beyond the extent of the tubes is also unreasonable (shown in Fig. 5.10). Thus, two values are used for the width of the back plane: pitch times four and pitch times five. Although the back plane to tube center distance is easy enough to change, Fig. 5.11 suggests a value of 12 cm is very reasonable. This is the value used hereafter.

### 5.5.1 Annual TRNSYS Simulations

In order to evaluate a collector's performance, annual TRNSYS simulations are performed. Instead of focussing solely on the optical performance of the collector, a more encompassing approach is applied. Figure 5.7 shows the annual energy collected by the collector ($Q_{coll}$). This is the amount of radiation the collector absorbs during the annual simulation. It considers only the optics of the collector and does not consider the losses to ambient. The analysis here includes losses since it has been shown that losses from the collector's manifold are very significant (eqn. (5.5)), and these losses increase with a longer manifold (eqn. (5.6)). The collector's performance is based on the term $\Sigma Q_{deliv}$. This is the amount of energy delivered annually by the collector during regular draws. The regular draws are similar to the SRCC Draw Profile. Namely, 71.8 liters of water are drawn through the collector three times a day: 7 AM, noon and 5 PM. $Q_{deliv}$ is the energy delivered during each of these draws:

$$Q_{deliv} = \int \dot{m} C_p (T_{out} - T_{in}) dt = m C_p (\overline{T}_{out} - \overline{T}_{in}) \tag{5.7}$$

where $\dot{m}$ is the flow rate of water delivered (kg/s) and $C_p$ is the specific heat of the water. The annual energy delivered ($\Sigma Q_{deliv}$) is simply the sum of all $Q_{deliv}$ over the year.

In the analysis, four collector tubes are used. Five tube pitches are used together with four back planes to give 20 data points (given in Table 5.3). The specular back plane is polished stainless steel while the diffuse back plane is simply a white surface. The total hemispherical reflectances chosen (0.6 and 0.7) are representative values for weathered materials. Although more exotic materials can be used for the back plane reflector to provide increased performance, a detailed Life Cycle Cost analysis is required to justify the increased cost of such materials.

**Table 5.3** Five Pitches and Four Back Planes Used in Annual TRNSYS Simulations

| Pitch [cm] | Back Plane Description |
|---|---|
| 14 | width = 4*p, $\rho_s = 0.6$ |
| 18 | width = 5*p, $\rho_s = 0.6$ |
| 22 | width = 4*p, $\rho_d = 0.7$, $r_d = 1.0$ |
| 26 | width = 5*p, $\rho_d = 0.7$, $r_d = 1.0$ |
| 30 | |

Figure 5.15 illustrates the annual energy delivered ($\Sigma Q_{deliv}$) by each of these collectors. The diffuse back planes provide the greatest increase in energy delivered at a large pitch. By increasing the pitch from 14 cm to 22 cm, approximately an 18% increase

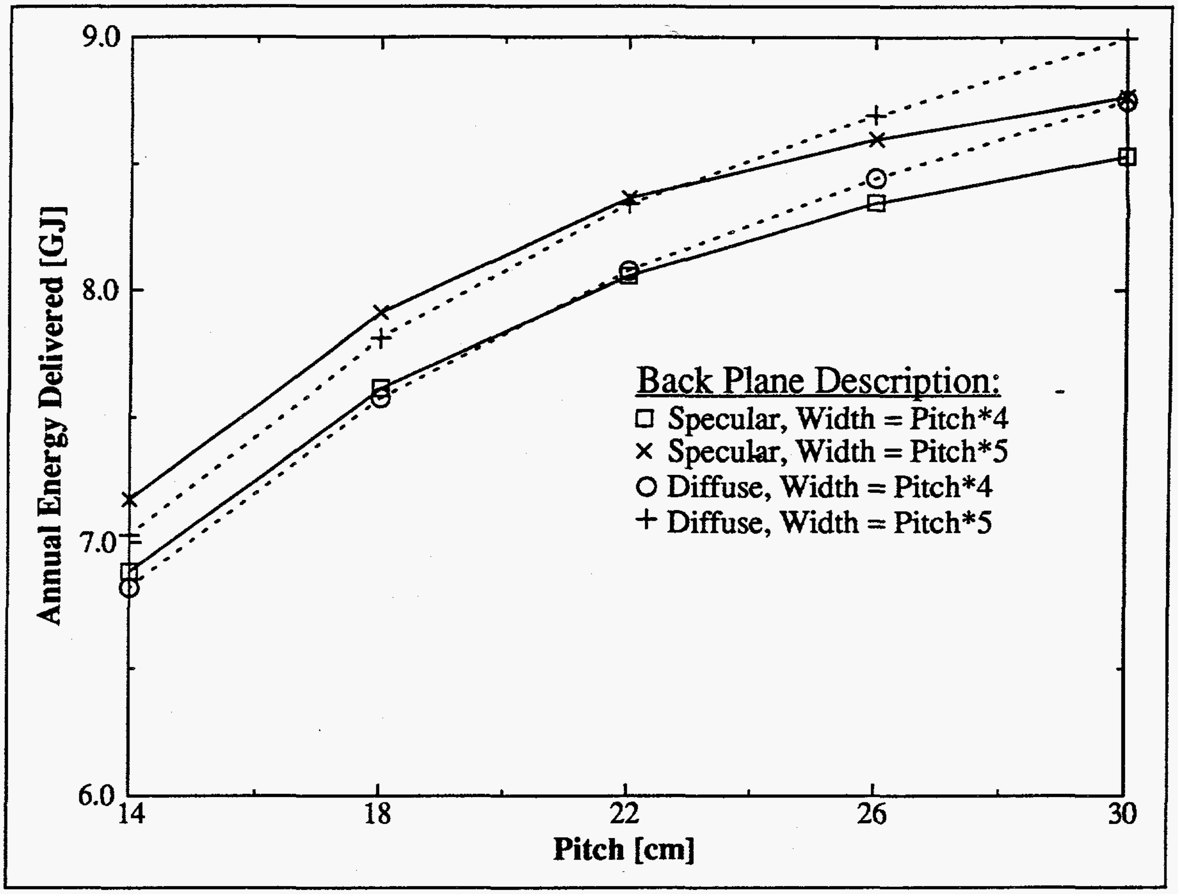

**Figure 5.15** Annual Energy Delivered by Four-Tube Collectors

in energy delivered is predicted for the diffuse back plane, while only a 16% increase is predicted for the specular back planes. Increasing the pitch beyond 22 cm produces a significantly smaller increase in energy delivered for both the specular back plane and the diffuse back plane (6% and 8% respectively). Two additional runs were made to assess whether or not the increased performance of the diffuse back plane at pitches greater than 22 cm is due to the increased reflectance of the diffuse back plane. With a pitch of 30 cm, a specular back plane ($\rho_s = 0.7$) outperforms the diffuse back plane ($\rho_d = 0.7$) by 1.4%. Similarly, with a pitch of 30 cm, a specular back plane ($\rho_s = 0.6$) outperforms a diffuse back plane ($\rho_d = 0.6$) by 0.8%. Consequently, it is more important to pick the back plane with the greater reflectance than it is to decide between diffuse and specular.

The increased width of the back plane consistently provides a 3% to 4% increase in energy delivered over that delivered for the narrower back plane.

It appears that the collector with the best performance would have a diffuse back plane and a large pitch (> 30 cm). However, a large pitch requires additional considerations. In addition to the obvious bulkiness a large pitch creates, many consider the larger tube spacing to be less aesthetically pleasing. A trade off between these issues and the diminishing return on performance must be made. In addition, a decision must be made concerning the width of the back plane. Again, aesthetics may play a role in the design process.

The next section provides more insight into the analysis of cylindrical solar collectors by considering the cost of various individual components.

### 5.5.2 Cost Analysis

The optimization encompasses both performance and economics. The simple metric for optimization used here is the ratio of annual performance to initial cost. Some costs are the same for all the collectors (tube cost), while others vary with the collector's geometry (back plane cost). Table 5.4 provides cost estimates for some of the collector components. These estimates were provided by Sun Utility Network, noting that the cost of the

**Table 5.4** Cost Estimates of Various Collector Components

| Component | Cost |
|---|---|
| Single Collector Tube (NEG Sun Tube) | \$90 |
| Stainless Specular Reflector ($\rho$=0.6) | \$45/m$^2$ |
| White Diffuse Reflector ($\rho$=0.7) | \$30/m$^2$ |
| Four Tube Manifold | \$60 |

diffuse reflector is much more of a guess than that for the other components. There are significant costs in addition to those provided in Table 5.4 (i.e. framing, insulation, shipping, installation, etc.) which vary with the collector's geometry, however a study including these costs is beyond the scope of this analysis.

Figure 5.16 illustrates the collector cost divided by the annual energy delivered by the collectors with geometries described in the previous section. Recall that only certain collector costs are being considered. The collectors with specular reflectors provide energy at an increased ratio of collector cost to annual energy delivered, primarily due to the higher cost of the stainless steel back plane. In fact, this ratio increases beyond a pitch of 22 cm, because the increase in the amount of energy delivered cannot compensate for

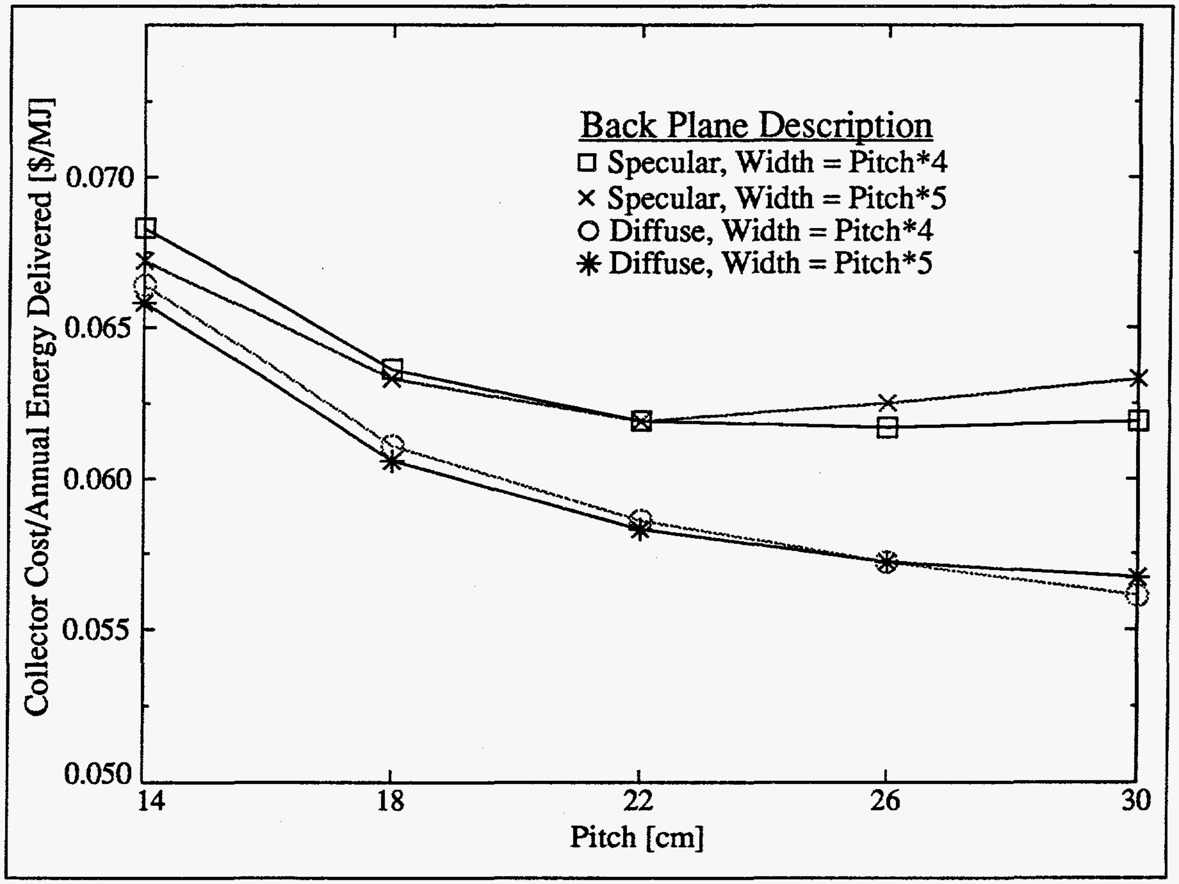

**Figure 5.16** Predicted Cost of Energy for an Annual Simulation

the increase in the cost of the reflector. The collectors with diffuse reflectors continue to provide a better performance ratio beyond a pitch of 22 cm, however the curve is clearly flattening.

Two NEG Sun Family collectors are mounted on the test bed at SEAL. The older of these collectors does not have a back plane reflector (assumed reflectance of 0.15, approximately that of a shingled roof) while the newer one ("unit tested" described in Table 4.1) has a polished stainless steel reflector. Performing annual simulations on these two collectors and dividing by the cost of the collector (using Table 5.4) gives an idea of how valuable this design procedure can be. The older collector delivered a cost to annual energy ratio of $0.078/MJ while the newer collector delivers a ratio of $0.083/MJ. This implies the cost of a reflector can not be justified with a pitch of approximately 15 cm. Viewing the curves in Fig. 5.16 shows the value of an increased pitch and a back plane reflector.

## 5.6 Summary

This chapter has provided verification of the validity of the computed IAM's for cylindrical solar collectors. In addition to an analytical verification, the results of the experimental tests have shown very good correspondence to predicted performance. Because of the many economic issues involved, the best collector geometry is not well defined. It is clear however that increasing the tube pitch in conjunction with the use of a back plane reflector provides a significant enhancement in the collector's performance and produces energy at a decreased cost. A specular reflector outperforms a diffuse reflector of the same reflectance. However, the cost of a specular reflector with a reflectance as high as the reflectance of white paint ($\rho = 0.7$) is an issue. It is also clear that increasing the pitch beyond a certain point will provide energy at an increased cost. A detailed Life Cycle Cost analysis is recommended to determine the optimal geometry.

# CHAPTER 6 CONCLUSIONS AND RECOMMENDATIONS

## 6.1 Summary

This study analyzed the optical performance of cylindrical solar collectors. The Monte Carlo method was employed in a Fortran 90 code used to compute the IAM's for cylindrical solar collectors. The code provides accurate results quickly and efficiently. Figure 6.1 illustrates the execution rate on various computer platforms. Approximately

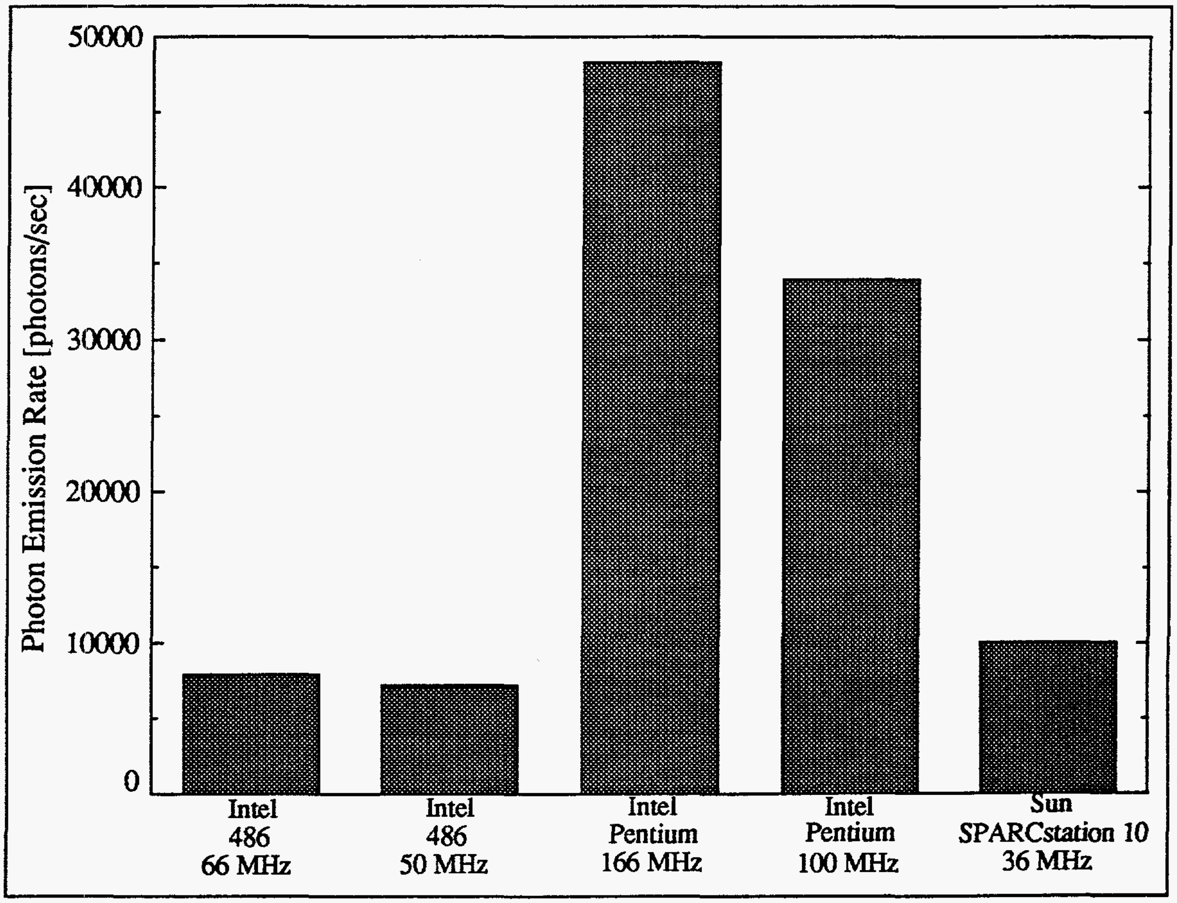

**Figure 6.1** Photon Emission Rate on Various Platforms

two million photons are emitted for an entire run for the 50 incident directions to achieve 1% convergence. Calculation of the hemispheric IAM's then takes from one to five minutes depending on the geometry of the collector and the computer hardware. The highlights of this new code include:

- simple input deck
- sufficiently complex material models to model "real" surfaces
- requires only 2% of the CPU time as the previous code by Knapmiller [1991] and Menon [1994]
- portability, by virtue of it being written in ANSI Fortran 90, executables are available for Sun and Windows platforms at URL: http://www.ColoState.EDU/Orgs/SEAL/research/IAM/iam.html
- analytically verified IAM's
- experimentally verified IAM's
- parameter variation study provides enhanced confidence in the computed IAM's

Using the results of the parametric variation study, a performance analysis commenced. This design procedure focussed on the tube pitch, back plane reflectance and back plane width. These are parameters which can easily be modified and have a significant impact on the collector's performance. In addition to the annual performance of the collector, a simplified cost analysis illustrated the economic value of changes in the collector's geometry. However, to keep the analysis simple, significant costs were neglected (shipping, packaging, installation, etc.), and the optimal collector must consider all of these costs. From the simple cost analysis performed, trends emerged. The results of this analysis include:

- the optimum tube pitch is approximately 22 cm, which represents the “knee” of the performance curve
- at larger pitches, a diffuse, white-painted back plane outperforms a specular, stainless steel back plane due to a higher hemispheric reflectance
- a diffuse back plane produces energy at a lower cost due to the lower cost of the back plane material

## 6.2 NEG Sun Family Collector Design

Although this study considers cylindrical solar collectors in general, the NEG Sun Family collector has been used exclusively in the experiments. This collector would benefit significantly from modifications to its geometry. The long-term hemispheric solar reflectance of the back planes is a concern. While stainless steel is durable, its reflectance ($\rho = 0.6$) is not the best. Specular materials, such as coated aluminum, can provide a reflectance as high as 0.82 after five years of outdoor exposure tests. Again, the use of more exotic materials requires a detailed Life Cycle Cost analysis to justify their use.

In addition to the collector design of ICS collectors such as the NEG Sun Family collector, a system design is equally important. Increasing the tube pitch and the use of a back plane reflector increases the amount of radiation incident on the collector tubes. Care must be taken that the thermal storage of the collector tubes is large enough to contain all this energy, else a change of phase (boiling) might result. Another issue is the type and amount of manifold insulation. Recall Fig. 4.1, which illustrates the deterioration in the spray foam insulation used to insulate the manifold. Most pipe insulation is not designed to withstand temperatures above the boiling point of water. Allowing the collector temperature to rise much above 100°C can have a serious effect on the integrity of the insulation. In addition, more insulation is desirable, in that the losses from the manifold constitute a significant portion of the collector losses.

Considering the issues above, the following recommendations are made:

- increase the tube pitch to approximately 22 cm
- use an inexpensive, yet durable back plane reflector, coated with a highly reflective, diffuse white paint
- increase the amount of manifold insulation

Determining the ideal tube pitch and back plane material requires a detailed cost analysis and a thorough investigation of the reflective materials available.

## 6.3 IAM Program Modifications

The new IAM program is satisfactory for studying simple collector geometries. The validity of the calculated IAM's for these geometries has been illustrated. There are however geometries which can not be simulated using the current version of the program. The following modifications to the IAM program will make it a more robust and useful tool:

- allow for the collector tubes to be tilted relative to the x-y plane
- permit the use of general planar surfaces
- enable the use of a finned tube collector in addition to a cylindrical absorber

# REFERENCES

Burns, P.J. and D.V. Pryor, 1989, "Vector and Parallel Monte Carlo Radiative Heat Transfer Simulation," *Numerical Heat Transfer, Part B: Fundamentals*, vol. 16, no. 1, pp. 97-124.

Duffie, J. A., and W. A. Beckman, 1991, *Solar Engineering of Thermal Processes, 2nd Edition*, John Wiley & Sons, New York.

Installation, Operation and Maintenance Manual, 1990, EG&G Flow Technology, Phoenix, Arizona.

Klein et al., 1994, "TRNSYS - A Transient System Simulation Tool, Ver. 14.1," Solar Energy Laboratory, University of Wisconsin, Madison, WI.

Knapmiller, K., 1991, "Computation of Total Hemispheric Incident Angle Modifiers for Solar Collectors," MS Thesis, Department of Mechanical Engineering, Colorado State University, Fort Collins, CO.

Maltby, J.D., 1990, "Analysis of Electron Heat Transfer via Monte Carlo Simulation," PhD Dissertation, Department of Mechanical Engineering, Colorado State University, Fort Collins, CO.

McIntire, W.R., 1982, "Factored Approximations for Biaxial Incident Angle Modifiers," *Solar Energy*, vol. 29, No. 4, pp. 315-322.

Menon, A., 1994, "Optical Performance of Cylindrical Absorber Collectors with and without Reflectors," MS Thesis, Department of Mechanical Engineering, Colorado State University, Fort Collins, CO.

Modest, M. F., 1993, *Radiative Heat Transfer*, McGraw Hill, New York, NY.

Perez, R., Seals, R., Anderson, J., Menicucci, D., 1995, "Calculating Solar Radiation Received by Tubular Solar Energy Collectors," *Solar Engineering - 1995: Proceedings of the ASME/JSME/JSES International Solar Energy Conference*, vol. 1, pp. 699-704, ASME, Maui.

Smith, T., 1997, "In-situ Parameter Estimation for Solar Domestic Hot Water Heating Systems Components," PhD Dissertation, Colorado State University, Fort Collins, CO.

Solar Rating & Certification Corporation, 1994, Directory of SRCC Certified Solar Collector and Water Heating System Ratings, Washington, D. C.

Sun Utility, 1997, personal communication.

Theunissen, P. and W. Beckman, 1985, "Solar Transmittance Characteristics of Evacuated Tubular Collectors with Diffuse Back Reflectors," *Solar Energy*, vol. 35, No. 4, pp. 311-320.

Window, B. and J. Zybert, 1981, "Optical Collection Efficiencies of Arrays of Tubular Collectors with Diffuse Reflectors," *Solar Energy*, vol. 26, pp. 325-331.

# APPENDIX A - IAM PROGRAM MANUAL

## A.1 General Description

This program computes a matrix of Incident Angle Modifiers (IAM's) for cylindrical solar collectors using three-dimensional Monte Carlo ray tracing. IAM's are defined as the ratio of a collector's performance at any angle of incidence [(tau-alpha)] to the collector's performance at normal incidence [(tau-alpha) normal]. The [(tau-alpha)] is defined as the ratio of photons absorbed by all collector tubes to the number of photons incident upon the aperture plane in the absence of tubes. Photons are traced in an enclosure through possibly many surface interactions until the photon is either absorbed by a surface or exits the volume of interest. The geometry of the collector cylinders is taken to be concentric with the inner cylinder being the collector tube and the outer cylinder being the glass cover. Any number of cylinders can be used with any spacing desired. The use of a back plane is also available for modeling reflected radiation from a roof or back plane reflector. An input deck (iam.in), using free-form input, where successive values input must be separated by one or more spaces, is used to define control information, material properties and collector geometry. An ampersand (&) may be used in the first column of a line to specify a comment line, ignored by the program. The following sections briefly describe the input for each the program.

## A.2 Units

It is important that all input be in a consistent set of units. Any consistent set of units can be used, for example cm, m, ft or in.

## A.3 Input Deck

The input deck is named "iam.in" and is written in free-form style. Suggested values are included in parenthesis at the end of the description.

Line 1 --- Title

| Item | Variable Name | Description |
|---|---|---|
| 1 | headin | title of the problem, may be up to 40 characters including spaces; must be left-justified, i.e. it is taken as the characters in columns 1 through 40. |

### Line 2 --- Control Information

| Item | Variable Name | Description |
|---|---|---|
| 1 | num_photons | number of photons emitted for each photon loop (10,000) |
| 2 | nplost_max | maximum number of lost photons permitted before execution of program is terminated (10) |
| 3 | num_ploops | maximum number of photon loops to be executed before moving on to next incident direction (100) |
| 4 | seed0 | initial seed to be used for the random number generator, if 0 is entered, a "random" initial seed is generated from the date and time of execution (0) |
| 5 | tol | desired tolerance for results (0.01) |

### Line 3 --- Directions and Materials

| Item | Variable Name | Description |
|---|---|---|
| 1 | n_long | number of longitudinal incident angles from which to emit photons (5) |
| 2 | n_tran | number of transverse incident angles from which to emit photons (10) |
| 3 | num_cyls | number of cylinders in collector array |
| 4 | num_surfaces | number of general surfaces (0, currently not available) |
| 5 | num_mats_surf | number of opaque surface materials to be read in the surface materials input section |
| 6 | num_mats_glass | number of semi-transparent materials to be read in the glass materials input section |

### Line 4 --- Print Control

| Item | Variable Name | Description |
|---|---|---|
| 1 | iprint | controls the amount of output sent to the output file "iam.out" (0)<br>iprint = 0 ===> minimal output is sent to iam.out<br>iprint = 1 ===> modest output is sent to iam.out<br>iprint =-1 ===> massive output is sent to iam.out |
| 2 | iprint_ran | controls the output of information regarding the random number generator, RNG (0)<br>iprint_ran = 0 ===> no RNG output<br>iprint_ran = 1 ===> the seeds used for initializing the RNG are sent to iam.out |
| 3 | idebug | controls the amount of debugging information sent to the output file "iam.dbg" (0)<br>idebug = 0 ===> no debug information sent to iam.dbg<br>idebug = 1 ===> modest amounts of debugging information is sent to iam.dbg<br>idebug =-1 ===> large amounts of debugging information sent to iam.dbg<br>idebug =-2 ===> massive amounts of debugging information sent to iam.dbg |
| 4 | idata | data check only flag (0)<br>idata = 1 ===> the whole input deck will be read, validity of the input data verified and execution of the program will be terminated - no IAM's |

will be calculated

idata = 0 ===> after the validity of the data is verified, normal execution of the program continues - IAM's will be calculated

| | | |
|---|---|---|
| 5 | iglass | a flag telling the program whether or not the collector cylinders will have glass covers (1) |

iglass = 1 ===> normal execution of the program occurs with the simulation of glass covers

iglass = 0 ===> the program is executed without glass covers around the collector cylinders (ro is taken as the radius of the uncovered absorbing cylinder)

Line 5 --- Aperture Plane Definition

| Item | Variable Name | Description |
|---|---|---|
| 1 | xmina | the x-value of the aperture plane minimum |
| 2 | xmaxa | the x-value of the aperture plane maximum |
| 3 | ymina | the y-value of the aperture plane minimum |
| 4 | ymaxa | the y-value of the aperture plane maximum |

Line 6 --- Back Plane Definition

| Item | Variable Name | Description |
|---|---|---|
| 1 | xminb | the x-value of the back plane minimum |
| 2 | xmaxb | the x-value of the back plane maximum |
| 3 | yminb | the y-value of the back plane minimum |
| 4 | ymaxb | the y-value of the back plane maximum |
| 5 | matnob | material number of the back plane |

Next "n_long" Lines --- Longitudinal Incidence Angles

| Item | Variable Name | Description |
|---|---|---|
| 1 | n | longitudinal incidence angle number |
| 2 | thetal(n) | longitudinal incidence angle |

Next "n_tran" Lines --- Transverse Incidence Angles

| Item | Variable Name | Description |
|---|---|---|
| 1 | n | transverse incidence angle number |
| 2 | thetat(n) | transverse incidence angle |

Next "num_cyls" Lines --- Cylinder Descriptions

| Item | Variable Name | Description |
|---|---|---|
| 1 | n | cylinder number |
| 2 | x0(n) | x-value of cylinder's origin |
| 3 | y0(n) | y-value of cylinder's origin |
| 4 | z0(n) | z-value of cylinder's origin |
| | | The origin of the cylinder is on the axis of the cylinder at the +x end of the cylinder. |
| 5 | length_cyl(n) | length of cylinder |
| 6 | ro(n) | outside radius of the glass cover (or radius of the absorber if iglass = 0) |
| 7 | ri(n) | radius of opaque, absorbing cylinder |
| 8 | betad(n) | angle of elevation of cylinder (degrees), currently not used |
| 9 | matno_glass(n) | material number of the glass cover |
| 10 | matno_cyli(n) | material number of the collector cylinder |

Next "num_mats_surf" Lines --- Opaque Surface Material Descriptions

| Item | Variable Name | Description |
|---|---|---|
| 1 | n | material number |
| 2 | rho_s(n) | specular reflectance of material n |
| 3 | rho_ss(n) | semi-specular reflectance of material n |
| 4 | rho_d(n) | diffuse reflectance of material n<br>0 <= rho_s + rho_ss + rho_d <= 1.0 |
| 5 | r_ss(n) | semi-specular weighting exponent (0 - 10) |
| 6 | r_d(n) | diffuse weighting exponent (1) |

Next "num_mats_glass" Lines --- Semi-transparent Surface Materials

| Item | Variable Name | Description |
|---|---|---|
| 1 | n | glass material number |
| 2 | n_glass(n) | index of refraction for glass material n (1.5) |
| 3 | k_glass(n) | extinction coefficient for glass material n (0.13/cm) |
| 4 | t(n) | thickness of glass material n |

It is very important that the product of the extinction coefficient and the glass thickness be dimensionless. The extinction coefficient will range from 0.04/cm for "water white" glass to 0.32/cm for "green glass." Soda-lime glass, with a normal transmittance of 0.9, has an extinction coefficient of approximately 0.13/cm.

## A.4 Execution of IAM Program

With the executable file "iam.exe" (simply "iam" for UNIX) and the input deck "iam.in" in the same directory, the program is executed by typing "iam" and pressing the RETURN or ENTER key. On Windows systems, the program can alternatively be executed by double-clicking on its icon. Output to the screen will be information about the current status of the program's execution. After each photon loop is completed, a line of information is written to the screen. This includes:

| Item | Description |
|---|---|
| 1 | whether or not the results have converged for this incident direction |
| 2 | current incident direction number |
| 3 | photon loop number for this incident direction |
| 4 | number of photons emitted in the photon loop |
| 5 | current convergence tolerance |
| 6 | desired convergence tolerance |

Upon completion of the program, the final photon tallies for each incident direction are written to the screen:

| Item | Description |
|---|---|
| 1 | direction number |
| 2 | transmittance-absorptance product (tau-alpha) |
| 3 | number of photons absorbed by the cylinders |
| 4 | number of photons absorbed by the glass covers |

## A.5 Output Files

During the execution, a number of files are written to the active directory:

| File Name | Description |
|---|---|
| iam.tab | contains tables of incidence angles and IAM's formatted for input into TRNSYS; also contains selected collector parameters sufficient to identify completely the geometry (these although present, are ignored by TRNSYS) |
| iam.out | contains information about the input deck, material properties, collector geometry, detailed results for each incident direction and detailed results for the entire run, including error termination information |
| iam.dbg | contains detailed information about ray-tracing calculations, if a debugging option is selected |
| iam.tmp | currently not used |
| iam.plt | contains data used to plot the collector geometry and photon emissions, currently not used |
| iam.lst | currently not used |

## A.6 Access to the IAM Program

The following files are available at CSU's Solar Energy Applications Laboratory web page (http://www.ColoState.EDU/Orgs/SEAL/research/IAM/iam.html):

| File Name | Description |
|---|---|
| manual | text file of this manual |
| iam.f90 | complete source code written in ANSI Fortran 90 |
| iam.in.1 | sample input file with four collector tubes, copy this file to "iam.in" to execute the program with this input deck |
| iam.in.2 | sample input file with eight collector tubes, copy this file to "iam.in" to execute the program with this input deck |
| iam.tab.1 | results of running the program with iam.in.1 as the input deck |
| iam.tab.2 | results of running the program with iam.in.2 as the input deck |
| iamdos.exe | executable which can be run under Windows |
| iamsun.exe | executable which can be run on a Sun platform |

# APPENDIX B - TRNSYS INPUT DECK

## B.1 Introduction

This appendix gives a listing of the TRNSYS input deck used to perform annual TRNSYS simulations on a cylindrical solar collector. A very similar input deck is used to perform the daily TRNSYS simulations to match the experimental values with the predicted values.

## B.2 Input Deck

```
*************************************************************
*              ***** Logical Units *****
ASSIGN ENERGY.LST 6
ASSIGN ENERGY.OUT 8
ASSIGN SAC.DAT   10
ASSIGN IAM.DAT   13
*
EQUATIONS 4
*              ***** Simulation Parameters *****
DAY   =    1
START =    0
STOP  = 8760
STEP  =  1/12
*
****************************************************************
SIMULATION START STOP  STEP
LIMITS 50 30 20
TOLERANCES 0.01 0.01
*WIDTH 132
*
****************************************************************
*
*             *****Computed Incident Angle Parameters*****
EQUATIONS 31
* Y intercept (tau-alpha normal)
TALN =  0.6179
* On-center Tube Spacing [m]
PITCH = 0.154
*
*            *****System Parameters*****
```

```
*
PI = 3.141593
*
* Collector fluid specific heat (kJ/kg-K)
CPF =  4.18
*
* Collector fluid density (Kg/m3)
RHOF =  1000.
*
* Collector Slope  (deg)
SLOPE =  45.
*
* Location Latitude (deg)
LATITUDE = 40.5
*
* Collector Azimuth (Deg)
AZIMUTH = 0.0
*
* Solar Constant (kJ/m2-hr)
SLRCST = 4871.
*
* Ground Reflectance
RHOG =  0.0
*
* Initial Incidence Angle
THETA = 45
*
* Number of Tubes
NTUBES = 8
*
*Initial Ambient Temperature
TI1 = 15
*
* Measured UA for Manifold (per meter of manifold)
UAMAN = 1.17*3.6
*
* Measured UA per Collector Tube
UATUBE = 0.55*3.6
*
* MEASURED TOTAL UA
UATOT = NTUBES*(UAMAN*PITCH + UATUBE)
*
* ESTIMATED BACK, EDGE, OTHER LOSSES
UABAK = UATOT/2.
*
* Number of nodes in ICS
NODES = 8
*
* Glazing Emmissivity
EGLAZ = 1.0
*
* TUBE CENTER TO ROOF DISTANCE (m)
RTDIST = 0.095
*
```

```
* DIAMETER OF ABSORBER TUBES (m)
DTUBE = 0.110
*
* DIAMETER OF GLAZING TUBE (m)
DGLAZ = 0.126
*
* LENGTH OF ABSORBER TUBES (m)
LTUBE = 2.016
*
* Top Area of ICS System (m2)
APERTURE = NTUBES*PITCH*LTUBE
*
* Top Heat Loss Coefficient (kJ/hr-m2-K)
UTOP =  (UATOT-UABAK)/APERTURE
*
* Solar Storage Volume  with tank cap. added (m^3)
VOLSOL = LTUBE * PI * NTUBES * (DTUBE ** 2) / 4.
*
* Initial ICS Temperature
TICS = 15
*
* Roof Reflectance
RFREFL = 0.0
*
* Ambient Pressure
PRESSURE = 1000
*
* Cloud Emmisivity
ECLOUD = .9
* Sky Temperature
TSKY = 15
*
***** Water Mains Temp. Forcing Function *****
*
UNIT 14 TYPE 14 WATER MAINS TEMP. PROFILE
PARAMETERS 48
0,11.33      744,11.33   744,14.28  1416,14.28   1416,14.78   2160,14.78
2160,17.33  2880,17.33  2880,19.22  3624,19.22   3624,20.72   4344,20.72
4344,21.78  5088,21.78  5088,23.0   5832,23.0    5832,21.44   6552,21.44
6552,20.17  7296,20.17  7296,15.78  8016,15.78   8016,11.78   8760,11.78
*
***** Radiation Processor *****
*
UNIT 16 TYPE 16 RADIATION PROCESSOR
PARAMETERS 8
* Horiz-Mode Track-Mode Tilt-Mode  Day  Latitude  Solar-Constant
SHIFT  Smooth
       3          1         1      DAY  LATITUDE     SLRCST
0.      2
INPUTS 6
9,3  9,19   9,20    0,0     0,0    0,0
0.0  0.0    0.0     RHOG    SLOPE  AZIMUTH
*
***** Solar Collectors (ICS type)
```

```
****************************************
*
UNIT 46 TYPE 46    ICS COLLECTOR
PARAMETERS  21
NODES      CPF        RHOF       VOLSOL    APERTURE  UTOP       EGLAZ
TALN       2          4          UABAK     NTUBES     PITCH      DTUBE
DGLAZ      LTUBE      RTDIST     RFREFL    13.        10.        5.
*#NODES    CPF        RHO        VOL       ATOP       UTOP       EGLAZ
*TA        CMODE      OMODE      UABACK    #TUBES     STUBE      DTUBE
*DGLAZ     LTUBE      RTDIST     RFREFL    Log.Unit   #TRANS.    #LONG.
*
INPUTS 14
15,1  9,4  14,1  TSKY  9,6  16,6  0,0  16,9   0,0  16,2 16,3   0,0  16,8
16,7
 0.   TI1   TI1   TI1   3.    0.  RHOG THETA SLOPE  90   90  AZIMUTH  0.
0.
*Mdot Tamb  Tin  Tsky Vwind It,c Gndrf Theta Slope Solz Solaz Collaz
Id,t Ib,t
*
DERIVATIVES   NODES
TICS TICS TICS TICS TICS TICS TICS TICS
*INITIAL TEMPERATURES IN DEGREES C
*

UNIT 9 TYPE 9 DATA READER
PARAMETERS 29
*        TIME    TILT    HORIZ  TAMB   TDEW    ??      ??        ??
2  8  1  1 1 0  -2 1 0  -3 1 0  4 1 0  5 1 0  6 1 0  7 0.1 0  8 0.1 0
10 -1
*
*$ SRCC DRAW PROFILE

UNIT 15 TYPE 14 NORMALIZED SRCC LOAD PROFILE
PARAMETERS 28
 0,0       7,0    7,71.8   8,71.8    8,0      12,0      12,71.8
13,71.8   13,0   17,0     17,71.8   18,71.8   18,0      24,0
*Draw Values are in kg/hr (56.9 gal/day)
*
* Energy Integrator
UNIT 24 TYPE 24 QUANTITY INTEGRATOR
INPUTS 2
46,3  46,2
0.0   0.0
*
UNIT 25 TYPE 25 RESULTS PRINTER
PARAMETERS 4
1 START STOP  8
*
INPUTS 2
24,1     24,2
Q-Deliv  Q-Coll
*
*
END
```